Surfaces and Interfaces 76 (2025) 107825

Contents lists available at ScienceDirect

Surfaces and Interfaces

journal homepage: www.sciencedirect.com/journal/surfaces-and-interfaces

Therapeutic potential of Coleus amboinicus mediated green caesium carbonate nanoparticles: A combined experimental and computational approach

Yuvaraj Dinakarkumar [a,*], Panneerselvam Theivendren [b,*], Hamad Al Lohedan [c], Krishnakumar Ramya [d], Kiruthika Jevanantham Senthamarai [e], Selvaraj Arokiyaraj [f], Jothi Ramalingam Rajabathar [c,**]

[a] Department of Biotechnology, School of Life Sciences Chennai, Vels Institute of Science, Technology and Advanced Studies (VISTAS), Tamil Nadu, India
[b] Department of Pharmaceutical Chemistry & Analysis, School of Pharmaceutical Sciences, Vels Institute of Science, Technology & Advanced Studies, Pallavaram, Chennai, Tamilnadu, India
[c] Chemistry Department, College of Science, King Saud University, P.O. Box. 2455, Riyadh, 11451, Kingdom of Saudi Arabia
[d] Department of Biotechnology, Vel Tech High Tech Dr. Rangarajan Dr. Sakunthala Engineering College, Avadi, Chennai, Tamil Nadu, India
[e] Department of Biotechnology, Saveetha School of Engineering, Saveetha University (SIMATS) Thadalam Chennai, Tamil Nadu 601205 , India
[f] Department of Food Science & Biotechnology, and Carbohydrate Bioproduct Research Center, Sejong University, South Korea

ARTICLE INFO

Keywords:
Green synthesis
Caesium carbonate nanoparticles
Coleus amboinicus
Antioxidant activity
Antibacterial efficacy

ABSTRACT

This study investigates the green synthesis and multifunctional bioactivities of caesium carbonate (Cs_2CO_3) nanoparticles (NPs) using *Coleus amboinicus* leaf extract rich in flavonoids, alkaloids, and phenolics. The eco-friendly synthesis eliminates toxic reagents while harnessing bioactive phytoconstituents for therapeutic potential. The synthesized NPs were characterized by UV–Visible spectroscopy (λ_max at 288 nm), FTIR (identifying functional groups such as O–H, *C = O*, and C–O), and SEM, which revealed irregular morphology with particle sizes ranging from 75 to 110 nm. Molecular docking studies demonstrated strong binding affinities (–6.1 to –8.3 kcal·mol^{-1}) of Cs_2CO_3 NP-associated phytochemicals with target proteins involved in oxidative stress (MMP-9) and inflammatory pathways, with ADMET predictions confirming acceptable pharmacokinetic and safety profiles. Antioxidant activity assessed by the DPPH radical scavenging assay showed an IC_{50} of 84.64 μg·mL^{-1} for Cs_2CO_3 NPs compared to 28.01 μg·mL^{-1} for ascorbic acid. Total antioxidant capacity further confirmed significant free radical neutralization potential. Anti-inflammatory activity, evaluated via BSA denaturation inhibition (45.61 % at 500 μg·mL^{-1}) and protease inhibition (46.56 % at 500 μg·mL^{-1}), indicated potential application in managing inflammation-associated disorders. Antibacterial assays revealed notable zones of inhibition against *Escherichia coli* (up to 20 mm) and *Staphylococcus aureus* (up to 22 mm) at 60 μg·mL^{-1}, suggesting promising alternatives to conventional antibiotics. Collectively, these findings highlight the potential of *C. amboinicus*-mediated Cs_2CO_3 NPs as sustainable candidates for antimicrobial, antioxidant, and anti-inflammatory applications.

1. Introduction

The development of eco-friendly nanomaterials is a growing priority in surface and interface science, particularly for biomedical applications where material–biological interactions are critical. Conventional methods for nanoparticle synthesis often involve hazardous chemicals and energy-intensive steps, raising concerns about environmental impact and biocompatibility. As a result, green synthesis approaches using plant-based systems have gained traction, offering a sustainable route to nanoparticle fabrication through biologically active compounds that function as natural reducing and stabilizing agents [1–3]. Metal and metal oxide nanoparticles synthesized via plant-mediated methods often exhibit enhanced surface functionality, increased colloidal stability, and intrinsic therapeutic potential. Despite extensive work on silver, gold,

* Corresponding authors.
** Co corresponding author.
E-mail addresses: yuvarajd.sls@vistas.ac.in (Y. Dinakarkumar), panneerselvam.sps@vistas.ac.in (P. Theivendren), jrajabathar@ksu.edu.sa (J.R. Rajabathar).

https://doi.org/10.1016/j.surfin.2025.107825
Received 11 July 2025; Received in revised form 18 September 2025; Accepted 8 October 2025
Available online 9 October 2025

and zinc oxide nanoparticles, alkali metal-based nanomaterials such as caesium carbonate (Cs_2CO_3) remain underexplored. Cesium compounds are known for their physicochemical versatility, yet their green synthesis and interface behaviour with biological systems are poorly understood. Addressing this gap can provide new insights into how surface-modified alkali nanoparticles perform in biological contexts and contribute to multifunctional nanomedicine platforms [4]. These methods preserve ecological sustainability and access the healing abilities of plants. The research herein aims to develop nanoparticles using extracts from *Coleus amboinicus* (Lour.), commonly known as Indian borage or Cuban oregano, a perennial aromatic herb belonging to the family Lamiaceae. Widely cultivated in tropical and subtropical regions, it has long been used in traditional medicine for its diverse pharmacological properties, including antimicrobial, anti-inflammatory, antioxidant, and wound-healing activities. The plant is rich in bioactive phytochemicals such as phenolic acids, flavonoids, terpenoids, and essential oils, which contribute to its therapeutic potential and make it an attractive candidate for green synthesis of nanoparticles. Its high content of reducing agents facilitates the bioreduction of metal and inorganic salts into stable nanoscale structures, while its capping compounds enhance particle stability and bioactivity. Leveraging the phytochemical richness of *C. amboinicus* in nanomaterial synthesis offers a sustainable and eco-friendly alternative to conventional chemical routes, aligning with the growing demand for greener technologies in nanoscience and biomedical research [5,6]. One of the unique features of nanoparticles is their larger surface area and reactivity that helps them to interact effectively with biological systems. Green synthesis of Cs_2CO_3 nanoparticles provides an eco-friendly method to improve the efficiency of plant compounds as therapeutics. This study presents a novel approach to the green synthesis of caesium carbonate (Cs_2CO_3) nanoparticles using *Coleus amboinicus* extract, eliminating the need for toxic reagents and energy-intensive synthesis methods. While previous reports have explored plant-mediated nanoparticle synthesis, to our knowledge, this is the first study to integrate eco-friendly synthesis of Cs_2CO_3 nanoparticles with a comprehensive evaluation of their antioxidant, anti-inflammatory, antibacterial, and anti-tuberculosis activities, alongside detailed in silico molecular docking and ADMET profiling. This combined experimental–computational strategy not only advances understanding of the multifunctional therapeutic potential of Cs_2CO_3 nanoparticles but also provides mechanistic insights into their bioactivity. The unique integration of sustainable synthesis, broad-spectrum bioassays, and computational validation distinguishes this work from existing literature and contributes to the development of safe, eco-conscious nanomaterials for biomedical applications.

2. Materials and methods

2.1. Chemicals

Analytical-grade calcium carbonate (≥99 % purity, Sigma-Aldrich, Chennai, India; Cat. No. C6763) and cesium chloride (≥99 % purity, Sigma-Aldrich, Chennai, India; Cat. No. 289,329) were used as precursor salts for nanoparticle synthesis. All solvents, including distilled water, were of high-purity laboratory grade and freshly prepared prior to use. Unless otherwise stated, all reagents were employed without additional purification. Glassware was cleaned with detergent, rinsed thoroughly with distilled water, and oven-dried before experiments.

2.2. Target identification

The KEGG pathway hsa05235 is about "PD-L1 expression and PD-1 checkpoint pathway in cancer" of human. It explains how cancer cells highjack the PD-1/PD-L1 pathway to cripple immune system, specifically T-cell function. Such suppression goes along with PD-L1 overexpression in tumour cells through survival pathways such as MAPK and PI3K/Akt. Moreover, it describes the significance of anti-tumour function and immune evasion in cancer treatment using PD-1/PD-L1 interaction with antibodies blocking as well KEGG Pathway [7,8].

2.3. Ramachandran plot statistics

PDBsum is a database that provides detailed summaries and analyses of the experimentally-determined structures in the Protein Data Bank. This includes: Diagrams of protein structures (secondary structure elements, domain architectures, binding interactions) Returned in an annotated form Plane representation Protein-ligand interactions, including information about chemical stoichiometry and physico-chemical properties Plane representation Enzyme active sites all amongst ligands interacting in such a particular type to function, 2D diagrams of protein-protein. This new information will be useful to researchers in the field for molecular modeling, drug design and studying protein mechanisms [9,10]. Link https://www.ebi.ac.uk/thornton-srv/databases/pdbsum/ to additional resources for more detailed analysis of the protein structures is also provided in database.

2.4. Protein preparation

Proteins can be prepared using RCSB, PubChem, and CHARMM-GUI. The preparation process can be initiated by fetching the protein structure through RCSB-PDB (https://www.rcsb.org). The ligands .sdf file can be downloaded from PubChem (https://pubchem.ncbi.nlm.nih.gov). These files can then be imported to CHARMM-GUI (Web-based tool for setting up molecular dynamics simulations). The protein structure can be optimized, crystallographic water can be removed, and missing atoms can be added using the CHARMM-GUI interface. After the final setup has been completed, the system can be exported for additional molecular dynamics simulations [11–15].

2.5. In silico molecular docking and admet prediction

The in silico docking studies were performed to explore potential inhibitory interactions between selected dietary antioxidants, quercetin, carvacrol, and vitamin C and matrix metalloproteinase-9 (MMP-9), an enzyme implicated in inflammation, tissue remodeling, and microbial pathogenesis. These bioactive molecules were chosen because they are known constituents or analogs of phytochemicals present in Coleus amboinicus extract, which acts as the reducing and capping agent in Cs_2CO_3 nanoparticle synthesis. Their docking against MMP-9 aimed to simulate the possible biological effects mediated by the organic corona surrounding the nanoparticles. By evaluating the binding affinities and interaction profiles of these compounds with MMP-9, the study provides mechanistic insight into how the phytochemical-coated nanoparticles might exert antioxidant, anti-inflammatory, and antimicrobial properties at a molecular level. Ligand structures were retrieved from the PubChem database (https://pubchem.ncbi.nlm.nih.gov) in SDF format and energy-minimized using Chem3D 20.0. Protein structures were obtained from the Protein Data Bank (PDB) in PDB format, ensuring resolution <2.5 Å. All water molecules, ligands, and cofactors were removed using BIOVIA Discovery Studio Visualizer 2021, and polar hydrogens and Kollman charges were added using AutoDock Tools (ADT) v1.5.7.

Docking simulations were conducted using AutoDock Vina v1.2.0 with the Lamarckian Genetic Algorithm for conformational search. The grid box dimensions were set to encompass the active site residues identified from literature and CASTp 3.0 server predictions, with spacing of 1.0 Å. Each docking run generated nine binding poses ranked by binding energy ($kcal \cdot mol^{-1}$). The pose with the lowest binding energy and favorable hydrogen bonding or hydrophobic interactions was selected for further analysis.

The docked complexes were visualized and analyzed using PyMOL 2.5.0 and Discovery Studio, focusing on hydrogen bonds, π–π stacking, hydrophobic interactions, and key amino acid contacts. ADMET

properties were predicted using the SwissADME (http://www.swissadme.ch/) and pkCSM (http://biosig.unimelb.edu.au/pkcsm/) online servers, assessing parameters including Lipinski's rule of five compliance, gastrointestinal absorption, blood–brain barrier permeability, hepatotoxicity, and cytochrome P450 inhibition potential. All computational work was performed on a workstation running Windows 11 with an Intel® Core™ i7–12,700 processor, 32 GB RAM, and NVIDIA RTX 3060 GPU support [11–15].

2.6. Sample collection

Fresh leaves of *Coleus amboinicus* were collected from local sources in Avadi, Chennai (13.1067° N, 80.0970° E). The plant was taxonomically identified and authenticated by Plant Anatomy Reasearch Centre (PARC), West Tambaram, Chennai, Tamil Nadu, India. The leaves were shade-dried for one week to preserve phytochemicals, then ground into a fine powder using a sterilized mortar and pestle. The powder was stored in an airtight container at room temperature until extraction.

2.7. Extraction procedure

The powdered leaf material (5 g) was subjected to Soxhlet extraction using distilled water as the solvent. Extraction was carried out for 32 cycles under controlled heating to prevent thermal degradation of phytoconstituents. The aqueous extract was concentrated using a rotary evaporator (Buchi Rotavapor R-300) at 40 °C under reduced pressure to obtain a viscous residue. Extract yield was calculated as the weight of dry extract relative to the initial plant material [10,16].

2.8. Phytochemical screening of the extract

Qualitative phytochemical tests were performed following standard protocols to confirm the presence of alkaloids, flavonoids, terpenoids, steroids, phenols, glycosides, saponins, and tannins. All reagents used in screening were analytical grade [17,18].

2.9. Synthesis of caesium carbonate

2.9.1. Central composite design

Caesium carbonate nanoparticles were synthesized using a central composite design (CCD) to optimize precursor concentrations and reaction conditions. A 0.3 M calcium carbonate solution and 0.3 M caesium chloride solution were prepared separately using analytical-grade salts dissolved in distilled water. Equal volumes of these solutions were combined and added dropwise to 25 mL of *C. amboinicus* extract under constant stirring with a magnetic stirrer (IKA C-MAG HS 7) at ambient temperature (27 °C). The reaction mixture was covered with aluminum foil to avoid photodegradation and incubated for 24 h. The resulting precipitate was collected by centrifugation at 10,000 rpm for 15 min, washed three times with distilled water, and oven-dried at 50 °C. The dry powder was stored in sterile vials for further characterization using XRD, SEM, FTIR, and UV–VIS Spectrophotometer [19].

2.9.2. Characterization of synthesized nanoparticles

UV–Vis spectroscopy, a simple and cost-effective technique for nanoparticle analysis, was performed using a Systronics UV–Vis Spectrophotometer 117 (1 nm resolution, 200–800 nm range, 2 nm/s scan speed) [20]. FTIR spectroscopy (Jasco FT/IR-6600) was employed to identify functional groups, recording spectra from 400 to 4000 cm^{-1}. Morphology and elemental composition were examined using Field Emission SEM with EDS (Carl Zeiss Sigma). Samples were prepared by drop-casting 5 µL of nanoparticle suspension onto carbon-coated copper grids, blotting excess liquid, and air-drying. Crystalline structure, phase, and grain size were determined by XRD (single-crystal X-ray diffractometer, Model Tr-60), with crystallite size calculated using the Scherrer equation [21–24].

2.10. Bioactivity of biosynthesized caesium carbonate nanoparticles

2.10.1. Antioxidant assay

The DPPH Radical Scavenging Assay and Total Anti-oxidant Assay were used to determine the antioxidant activity of synthesized caesium carbonate nanoparticles from *Coleus amboinicus* leaves [25].

2.10.2. Total antioxidant assay

Biosynthesised caesium carbonate nanoparticles (Cs_2CO_3) underwent the total antioxidant activity. Different concentration sample (100µl) were added into the test tube (5 test tubes) for each sample, followed by 1 ml of the reagent blend (0.6 M sulphuric acid, sodium phosphate (28 mM) and ammonium molybdate (4 mM)) was added and shaken. The entire mixture is then incubated in bath water at 95 °C for 90 minutes. Immediately after the incubation, the samples were allowed to cool to room temperature and the optical density was recorded at 680 nm. The outcome was reported as ascorbic equivalence [25].

2.10.3. DPPH radical scavenging assay

Different concentrations of caesium carbonate nanoparticles (Cs_2CO_3) biosynthesized of 800 µl were taken and supplemented with 200 µl of 1 mM DPPH solution and were agitated sufficiently, the mixture was incubated for 30 min at room temperature. The absorbance was read at 517 nm after the incubation period to determine the IC_{50} value The DPPH scavenging activity percentage was determined by applying the below mentioned formula [26,27].

$$\textit{Percentage Inhibition} = \frac{A_c - A_1}{A_c} \times 100 \quad (1)$$

Where A_c is the absorbance of control and A_1 is the absorbance of test or standard sample.

2.10.4. Anti-inflammatory

It is determined using BSA Inhibition Assay, and protein inhibitory assay for the biosynthesized nanoparticle anti-inflammatory assay.

2.10.5. BSA inhibition assay

Nanoparticles that are synthesised were subjected to inhibition assay. To each of the samples 500 µl of BSA (Bovine Serum Album) was added, incubated for 10 min at room temperature and then add heat of 51 °C for 20 min and it was cooled Absorbance was read at 660 nm, using acetyl salicylic acid as positive control. The inhibition percentage of protein denaturation was calculated by using the following equation [28].

$$\textit{Percentage Inhibition} = \frac{A_c - A_1}{A_c} \times 100 \quad (2)$$

Where A_1 is the absorbance of the sample and A_c is the absorbance of the positive control.

2.10.6. Protease inhibitory assay

A 100 µl of sample was taken and for a Protease Inhibitory assay two volumes of BSA (Bovine Serum Albumin) 100 ml was added and incubated for 5 min at room temperature. To this 250 µl of trypsin was added and the mixture was allowed to be centrifuged. The supernatant was then obtained by centrifugation, and the absorbance was measured at 210 nm taking acetyl salicylic acid as positive control. The inhibition percentage was determined by means of the following formula [28].

$$\textit{PPercentage Inhibition} = \frac{A_c - A_1}{A_c} \times 100 \quad (3)$$

Where A_1 is the absorbance of the sample and A_c is the absorbance of the positive control.

2.10.7. Antibacterial assay

Antibacterial Assay was performed on sterilized Muller Hinton agar medium. The medium was poured in sterilized petri plates and solidified. The Gram-positive *Escherichia coli* Bacteria (MTCC 572) and Gram-negative Bacteria Staphylococcus aureus (MTCC 737) were adjusted to 0.5 McFarland to obtain 108 cells/ml. Soogaksu was swabbed on the agar plates. Wells were punched with a sterile well borer on the inoculated agar plates. Add 30, 60, 90 $\mu g \cdot mL^{-1}$ of prepared sample to each well and incubate the plates at 37 °C for 24 h. The measurement of the inhibition zone surrounding the wells is in mm after the incubation time. Amoxicillin was used as a positive control and DMSO and water were used as negative control [25].

2.10.8. MABA assay protocol

Stock solutions of Rifampicin in dimethyl formamide (DMF) (10mg/mL) were prepared, aliquoted and stored at −20 °C. Alamar dye (Invitrogen) was purchased. MAB (Alamar Blue) was used to perform an antimycobacterial bioassay. In short, representative colonies of M. tuberculosis H37Ra from Lowenstein-Jensen (LJ) slope were suspended in 1 mL distilled water and the turbidity was matched to McFarland tube No.1 (107 CFU/mL) and diluted 1:25 in 7H9 (Middlebrook 7H9 [Becon Dicinson] supplemented with 0.2 % glycerol, 0.1 % casitone and 10 % albumin-dextrose, pH 6.8) and used as inoculums. 100 µL of the bacterial suspension was added to each well of a micro titer plate with the Cs_2CO_3 nanoparticles in Middlebrook 7H9 sales medium to a final volume of 200 µL, and the ultimate focus of test Cs2CO3 nanoparticles ran from 31.25 µg/mL to 0.97 µg/mL. MG and a sterile control well- were also present. Plates were sealed with parafilm and incubated at 37 °C.20 µL of Alamar blue dye were added to the wells, after approximately 7-day incubation. The plates were re-incubated overnight. Bacterial growth was indicated by a change in color from blue to pink. MIC was defined as the lowest concentration of the drug not showing a color change and the ranges were 0.0047–0.0095(µg/mL) [29].

2.10.9. Statistical analysis

All experiments were conducted in triplicate, and the results are expressed as mean ± standard deviation (SD). Statistical analysis was performed using GraphPad Prism version 9.0 (GraphPad Software, San Diego, CA, USA). One-way analysis of variance (ANOVA) followed by Tukey's post hoc test was used to determine the significance of differences among the various extract treatments. A p-value of <0.05 ($p < 0.05$) was considered statistically significant.

3. Result and discussions

3.1. Target identification

Venn diagram illustrating the overlap of biological targets between *Coleus amboinicus* and various Gram-positive and Gram-negative bacteria.

The left circle, labelled *Coleus amboinicus* Target, indicates that this plant has 10 unique biological targets. The right circle, labelled Gram-positive & negative Bacteria Target, shows that bacteria collectively have 15,045 unique targets. The overlapping central section, labelled Common Target, reveals that *Coleus amboinicus* and the bacteria share 90 common targets. **MMP9** XDH CD38 MAOA CDK1 CAMK2B TNKS2 AXL EGFR PIK3R1 CSNK2A1 NEK2 MMP13 AKR1B10 ABCB1 TNKS ACHE PYGL MPG HSD17B1 ESRRA AURKB MMP12 GLO1 GPR35 AKR1B1 SRC AKR1C1 ABCC1 AKR1A1 ADORA2A MAPT PIM1 CDK6 NOX4 AVPR2 PARP1 FLT3 CA2 TOP1 MET AHR CYP19A1 CA9 GSK3B CA12 MMP3 CXCR1 DRD4 CDK2 TYR SLC22A12 ALOX15 MPO ABCG2 TTR PIK3CG SYK TOP2A IGF1R PKN1 INSR AKT1 AKR1C3 CA6 DAPK1 APP PTK2 AKR1C4 F2 CA5A APEX1 CA4 PLA2G1B MYLK TERT CA3 ESR2 CYP1B1 ALOX5 PLK1 ALK AKR1C2 ARG1 KDR PTPRS BACE1 ADORA1 CA1 MMP2. This diagram visually emphasizes the extent of shared biological pathways or proteins between the plant and bacteria, potentially signifying targets that *Coleus amboinicus* could influence in bacterial pathogens. The overlap suggests a basis for exploring *Coleus amboinicus* as an antibacterial agent, as the shared targets may play essential roles in bacterial survival or virulence [16]. Identifying such common targets can be valuable in understanding the plant's therapeutic potential and developing treatments that exploit these shared pathways Fig. 1.

3.2. Network pharmacology

The complex protein interaction network represents, likely visualized using the STRING database, which highlights connections between various proteins. Each circular node represents a protein, labelled with its name, such as **MMP9** AKT1 ABCB1 SRCGSK3BPARP1 KDR MMP2 MET CDK2 IGF1R CDK1 PIK3R1 ABCG2 TERT EGFR ESR2 CDK6 PTK2 TOP2A SYK CYP19A1 APP MPO MAPT FLT3 MAOAACHE NOX4 AXL PIK3CG CA4XDH AURKB TYR MMP3 CSNK2A1. The proteins are grouped and color-coded, possibly based on functional similarities, pathways, or cellular roles.

The black lines connecting the nodes signify predicted or known interactions between these proteins. These interactions may include direct physical bindings, co-expression patterns, or shared biological pathways.

The dataset presents network centrality metrics for several proteins, evaluating their role within a biological interaction network. Metrics include Degree (number of direct connections), Betweenness (a measure of a protein's influence over communication paths), Closeness (how quickly a protein can connect to others), Eccentricity (farthest distance to any other protein in the network), Eigenvector (a measure of influence within the network based on connections to highly connected proteins), Radiality (how central a protein is), and Stress (the number of shortest paths passing through the protein).

Proteins with high Degree values, such as MMP9 (50), AKT1 (42), and ABCB1 (38), are highly connected, suggesting key roles in maintaining network integrity. High Betweenness values for MMP9 and AKT1 imply that these proteins facilitate significant communication paths, making them crucial for network flow and potentially influential in cellular processes. Proteins with higher Closeness values, like MMP9 and ABCB1, can quickly interact with others in the network, indicating accessibility to other proteins.

Eigenvector centrality highlights the influence of proteins like MMP9 and AKT1, suggesting these are highly connected within clusters of important nodes. Radiality values, which are relatively high for these proteins, confirm their central position. Stress values further emphasize MMP9's role, as it appears frequently in shortest paths, reinforcing its potential impact on network dynamics and signaling pathways. These centrality measures suggest that MMP9, AKT1, and ABCB1 are pivotal nodes within the network, likely involved in critical biological functions [30] Table 1 and Fig. 2.

3.3. Mechanism of matrix metalloproteinase-9 (MMP-9)

Specifically, matrix metalloproteinase-9 (MMP-9) is important in combating against Gram-negative as well as Gram-positive bacterial infection [31]. MMP-9 is secreted by neutrophils and macrophages during infection and remodelling of the ECM (extracellular matrix) facilitates immune cell infiltration towards the infection locus. MMP-9 acts by breaking down the ECM barriers and helping leukocyte migrate to process an efficient pathogen targeting and elimination. Furthermore, MMP-9 help regulate the inflammatory response process by upregulating cytokines and chemokines that recruit even more immune cells. For Gram-negative pathogens [32] (such as *Pseudomonas aeruginosa* and *E. coli*), MMP-9 can degrade bacterial biofilms, which enhance the resistance of these pathogens to both the host immune response and antibiotic action. MMP-9 activity aids clearance in Gram-positive infections (for example, *Staphylococcus aureus*) by the

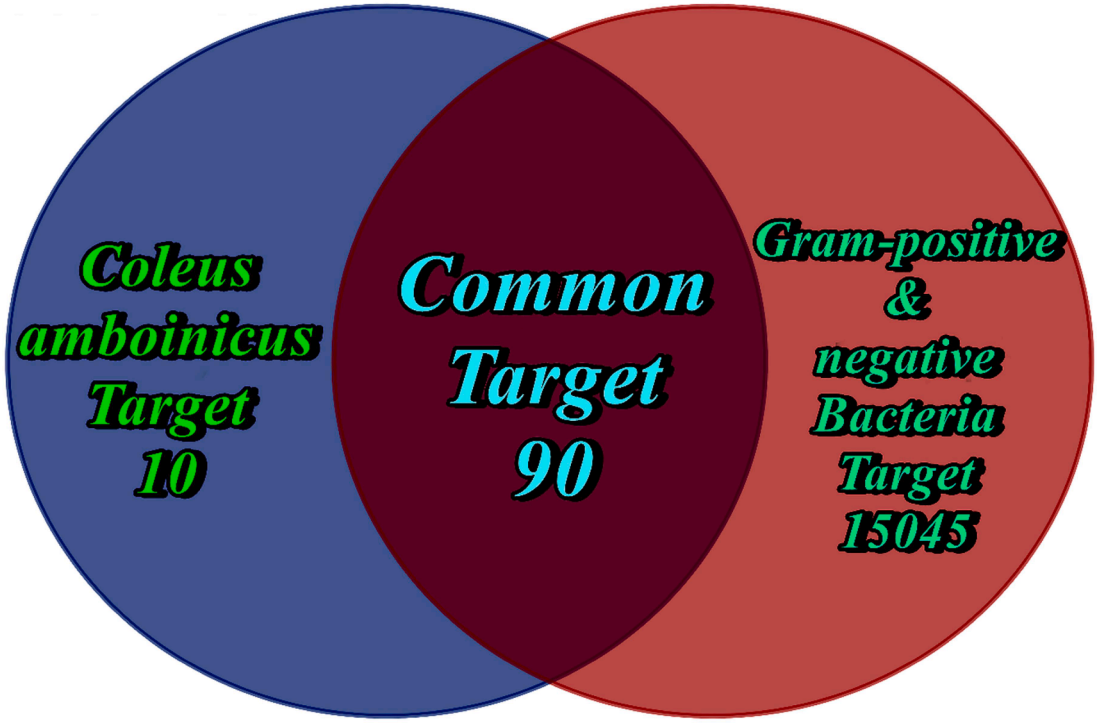

Fig. 1. Venn diagram illustrating the overlap of biological targets between Coleus amboinicus (10 unique targets) and Gram-positive/negative bacteria (15,045 unique targets), with 90 common targets shared between both groups.

Table 1
The network centrality metrics for key proteins, including Degree, Betweenness, Closeness, Eccentricity, Eigenvector, Radiality, and Stress. Metrics assess protein influence within biological interaction networks.

Protein	Degree	Betweenness	Closeness	Eccentricity	EigenVector	Radiality	Stress
MMP9	50	1665.8	0.00769	0.33333	0.30685	4.40449	7370
AKT1	42	992.918	0.00714	0.33333	0.28183	4.29213	4806
ABCB1	38	813.174	0.0068	0.33333	0.26059	4.21348	3706
SRC	33	437.577	0.00667	0.33333	0.24493	4.17978	2950
GSK3B	31	424.888	0.00658	0.33333	0.22677	4.1573	2490
PARP1	29	373.914	0.00633	0.33333	0.21571	4.08989	2522
KDR	25	263.549	0.00633	0.33333	0.2068	4.08989	1814
MMP2	24	188.956	0.00613	0.33333	0.19513	4.03371	1366
MET	20	38.566	0.00595	0.33333	0.19125	3.97753	404
CDK2	20	168.732	0.00585	0.33333	0.15245	3.94382	1388
IGF1R	20	28.9571	0.00595	0.33333	0.19165	3.97753	300
CDK1	18	74.3519	0.00578	0.33333	0.14725	3.92135	698
PIK3R1	18	28.8678	0.00578	0.33333	0.16217	3.92135	292
ABCG2	18	300.128	0.0061	0.33333	0.14775	4.02247	1868
TERT	17	93.6743	0.00578	0.33333	0.1503	3.92135	684
EGFR	17	117.448	0.00592	0.33333	0.15229	3.96629	1060
ESR2	16	329.291	0.00599	0.33333	0.13612	3.98876	1954
CDK6	15	42.8711	0.00562	0.25	0.13253	3.86517	458
PTK2	15	12.0729	0.00571	0.33333	0.15822	3.89888	160
TOP2A	15	95.5142	0.00552	0.25	0.10617	3.83146	716
SYK	14	21.5008	0.00556	0.33333	0.13248	3.8427	166
CYP19A1	14	238.869	0.00595	0.33333	0.10373	3.97753	1524
APP	14	53.8272	0.00575	0.33333	0.12866	3.91011	420
MPO	13	81.7787	0.00518	0.25	0.07621	3.69663	432
MAPT	13	124.957	0.00575	0.33333	0.10694	3.91011	886
FLT3	13	29.7276	0.00552	0.25	0.12308	3.83146	264
MAOA	13	339.167	0.00546	0.25	0.06073	3.80899	1634
ACHE	11	93.0196	0.00565	0.33333	0.07369	3.8764	652
NOX4	11	26.858	0.00562	0.33333	0.11323	3.86517	260
AXL	11	4.51604	0.00546	0.33333	0.11807	3.80899	46
PIK3CG	11	2.84024	0.00546	0.33333	0.11547	3.80899	36
CA4	11	403.399	0.00488	0.25	0.03996	3.5618	2556
XDH	10	92.7337	0.00538	0.33333	0.05942	3.77528	504
AURKB	10	14.9327	0.00478	0.25	0.06959	3.51685	114
TYR	10	52.5669	0.00559	0.25	0.08672	3.85393	412
MMP3	10	45.8738	0.00535	0.33333	0.08463	3.76404	292
CSNK2A1	10	35.5557	0.00549	0.33333	0.08192	3.82022	242

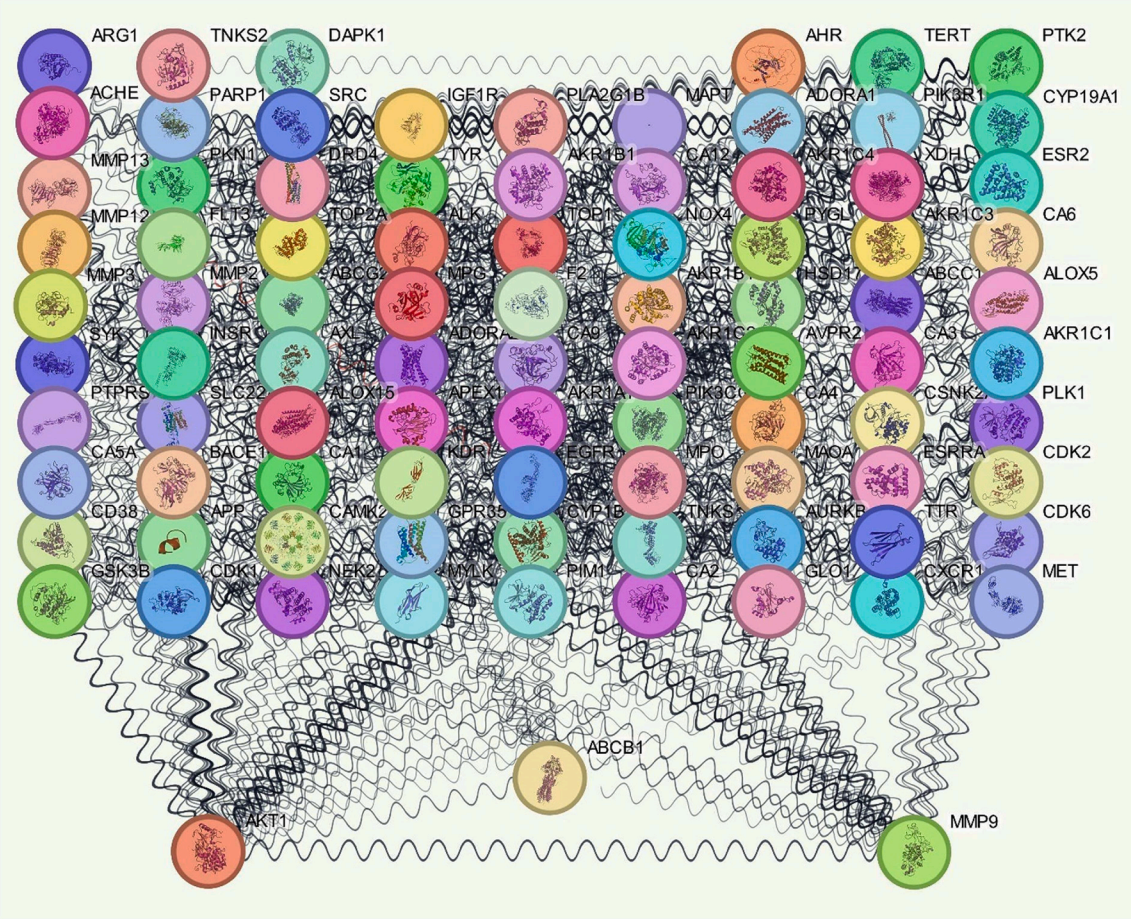

Fig. 2. Network diagram showing protein interactions, with nodes representing individual proteins and lines depicting connections. Color-coded clusters indicate functional groupings, emphasizing central proteins like AKT1, ABCB1, and MMP9.

removal of bacterial capsules. However, high levels of MMP-9 activity can cause harm to the tissue and worsen inflammation indicating a contradicting role of host defense as well as potential injury [33] Fig. 3.

3.4. Ramachandran plot statistics

The Ramachandran plot statistics and G-Factors provide insights into the quality of a protein structure model [34]. Out of 259 non-glycine, non-proline residues, 89.6 % fall within the most favored regions (A, B, L), 9.7 % are in additional allowed regions, and 0.8 % in generously allowed regions. Importantly, no residues are in disallowed regions, indicating a well-refined structure. This distribution suggests a high-quality model, as models of good quality typically have over 90 % of residues in the most favored regions. The total number of residues is 314, including 31 glycines and 20 prolines.

G-Factors assess the structure's stereochemical quality, with values below −0.5 indicating unusual conformations. The dihedral angle parameters show acceptable values, with an overall average score of 0.17, indicating generally favorable conformations. Main-chain covalent forces (bond lengths and angles) have a higher average score of 0.58, reinforcing the model's accuracy. The overall average G-Factor score of 0.34 suggests the structure is within expected norms, with no highly unusual values, signifying reliability in the stereochemistry and bond parameters [35].

Overall, these metrics confirm the structure's quality, with favorable residue conformations and reasonable covalent geometry, making it a reliable protein model Fig. 3.

3.5. Molecular docking

3.5.1. Quercetin-protein complex

The molecular interaction between Quercetin and its target protein is visualized in both 2D and 3D representations. The 2D interaction diagram reveals how Quercetin engages with specific amino acids in the protein's binding pocket. Hydrophobic contacts are depicted with red arcs, while other non-bonded interactions appear as red dotted lines. Several amino acids, including Gly205, Asn208, Leu209, and Val203, form close contacts with Quercetin, contributing to the stability of the complex. Hydrogen bonding interactions are shown as green dotted lines, with measured distances indicating their relative strengths.

The 3D visualization offers a spatial perspective of Quercetin positioned within the protein's active site. This representation emphasizes the three-dimensional arrangement of hydrogen bonds and other key interactions, shown as green dotted lines. The protein's structural elements, comprising alpha helices and beta sheets, are distinguished by different colors, highlighting how specific residues like Asn208 and Glu301 interact with the ligand. This spatial representation enhances our understanding of how Quercetin fits into the binding pocket, providing insights into its binding strength and potential biological activity Fig. 4.

3.5.2. Carvacrol-protein complex

The molecular interaction analysis of a ligand (Carvacrol) with a target protein, shown in both 2D and 3D representations. In the 2D interaction diagram illustrates the key interactions between Carvacrol and surrounding amino acids within the protein binding pocket. Red arcs with radiating lines around the amino acids indicate hydrophobic

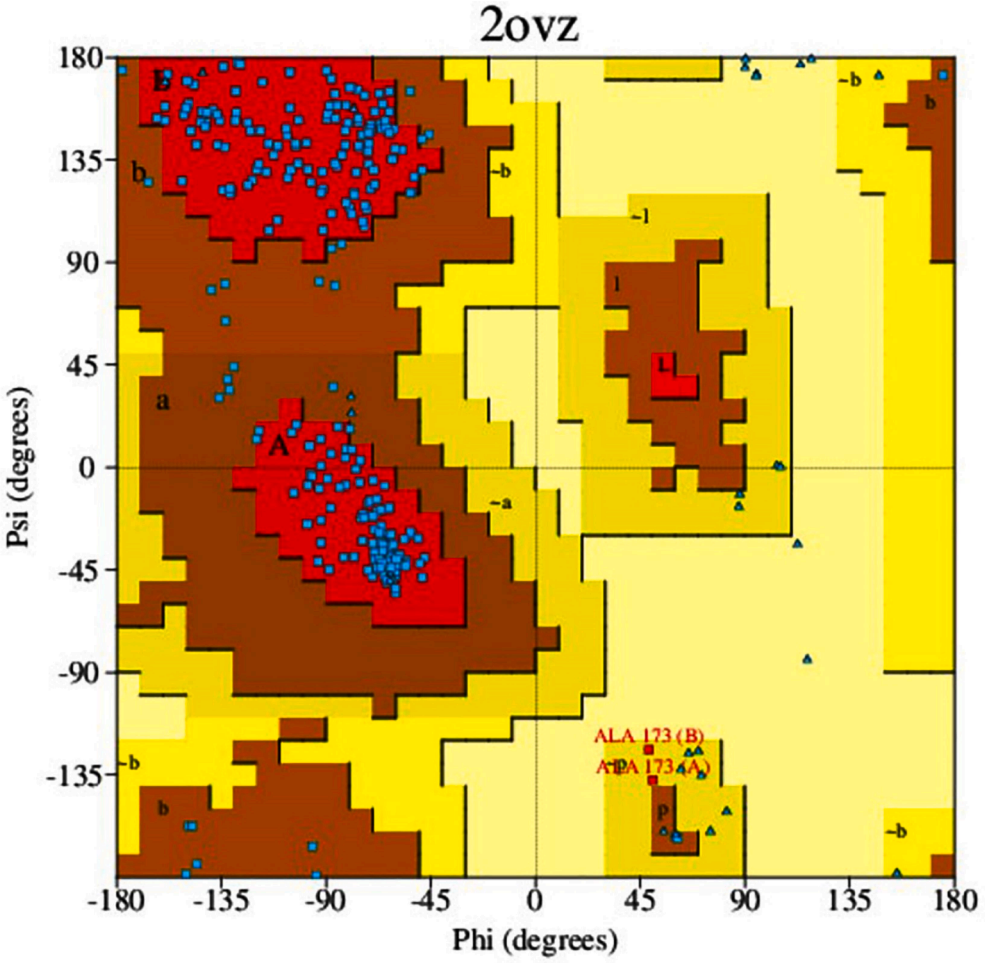

Fig. 3. Ramachandran plot for protein 2OVZ, showing psi (Ψ) and phi (Φ) angles for residues. Red regions indicate most favored conformations, brown additional allowed, yellow generously allowed, and light yellow disallowed.

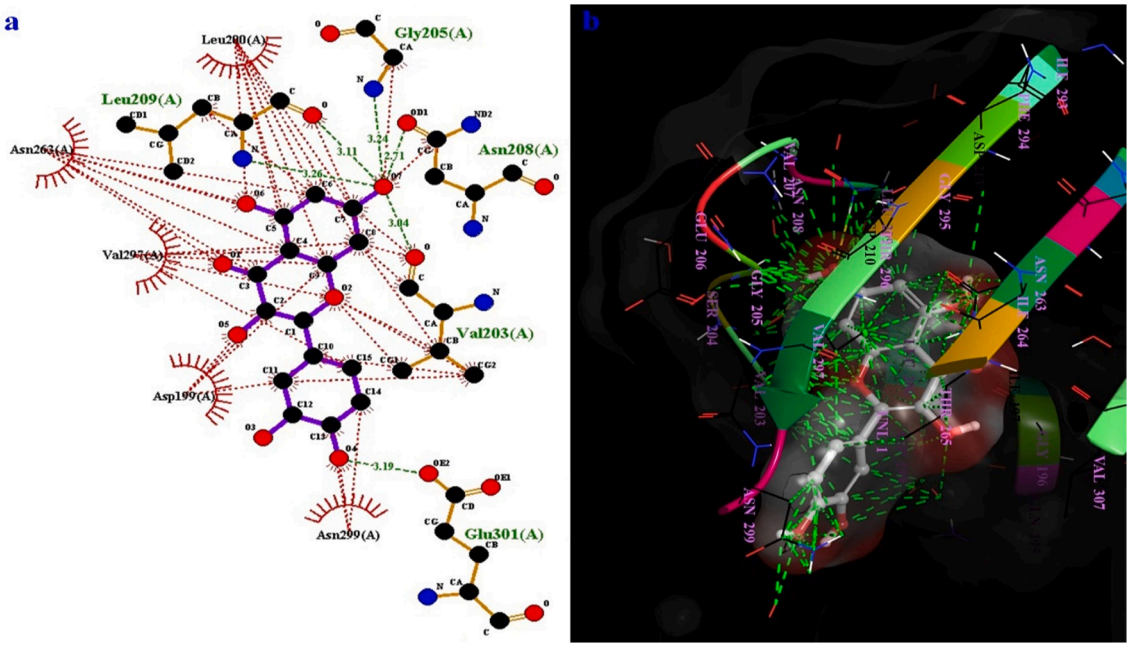

Fig. 4. (a) 2D interaction map and (b) 3D binding site view showing ligand-protein interactions of the 2OVZ-Quercetin, including hydrogen bonds (green dashed lines) and hydrophobic contacts (red arcs) with key residues in the binding pocket.

contacts, while red dashed lines show non-covalent interactions, such as hydrogen bonds, between the ligand and specific residues. In the 3D view of the ligand binding site provides a spatial visualization of Carvacrol within the protein. Green dashed lines represent hydrogen bonds and other significant non-covalent interactions that stabilize the ligand in the binding pocket. The protein residues forming contacts with the ligand are color-coded, with highlighted areas around key interacting residues including Asn208, Leu209, Gly205, Val297 Gly295, Asn208, and Val203. This visualization aids in understanding the binding orientation and interaction pattern, offering insights into the ligand's binding affinity and stability within the protein's active site Fig. 5.

3.5.3. Vitamin C -protein complex

The molecular interactions between a vitamin C ligand and a target protein, displayed in both 2D and 3D visualizations. In the 2D interaction diagram shows various types of non-covalent interactions between the ligand and surrounding amino acids in the protein binding site. Red arcs with radiating lines indicate hydrophobic interactions between the ligand and specific residues such as Met226, Val310, Ile228, and Gly193. Red dashed lines represent hydrogen bonds and other stabilizing interactions, with specific distances noted in green for precise hydrogen bonds involving residues like Gly227, Thr309, and Gly193, signifying the ligand's strong binding affinity. The 3D binding site, providing a spatial view of the vitamin ligand nestled within the protein's pocket. Green dashed lines indicate hydrogen bonds, while the color-coded helices and sheets of the protein structure help identify key residues interacting with the ligand, such as Leu200, Ser168, and Thr309. This three-dimensional arrangement highlights the orientation of the ligand and the geometry of the binding pocket, which are crucial for understanding the ligand's binding stability and interaction strength within the protein's active site. Together, these visuals offer valuable insight into the ligand-protein binding mechanism and potential biological activity Fig. 6.

3.6. Molecular dynamics

3.6.1. Quercetin-protein complex

The molecular dynamics simulation for the Quercetin-protein complex was performed under standard NPT ensemble conditions at 300 K for a total of 100 nanoseconds. The Root Mean Square Deviation (RMSD) analysis indicates a stable conformation of the protein throughout the simulation. The protein RMSD fluctuated within a typical range of 1–3 Å, suggesting the system reached equilibrium. The stability of the ligand within the binding pocket was confirmed by the Ligand RMSD, which remained close to that of the protein, implying that Quercetin maintained its binding pose and did not diffuse away.

The Root Mean Square Fluctuation (RMSF) analysis revealed localized flexibility along the protein chain. As expected, the N- and C-terminal regions exhibited higher fluctuations, while secondary structures like alpha-helices and beta-strands were more stable. Residues interacting with the ligand demonstrated lower RMSF values, suggesting a rigid binding environment around Quercetin, which may enhance binding stability.

Protein-ligand contacts were categorized into hydrogen bonds, hydrophobic interactions, ionic interactions, and water bridges. Hydrogen bonds were particularly prominent, with interactions involving residues such as Gly227 and Thr309, maintained for a significant portion of the simulation time. These hydrogen bonds are likely crucial for Quercetin's binding affinity. Hydrophobic interactions were observed with residues like Met226 and Val310, supporting ligand stability by creating a hydrophobic environment.

The secondary structure analysis showed that the protein maintained 59.95 % of its structure in alpha-helix and beta-strand forms, indicating structural integrity. Ligand flexibility was assessed through the Ligand RMSF, revealing those certain atoms in the ligand structure experienced minimal fluctuations, suggesting minimal conformational changes.

The torsion profile for Quercetin's rotatable bonds demonstrated stable torsional angles, indicating the ligand maintained a consistent conformation within the binding pocket. Additionally, ligand properties such as Radius of Gyration (rGyr) and Solvent Accessible Surface Area (SASA) supported the idea of an extended, stable conformation.

Overall, the simulation data suggests that Quercetin forms a stable

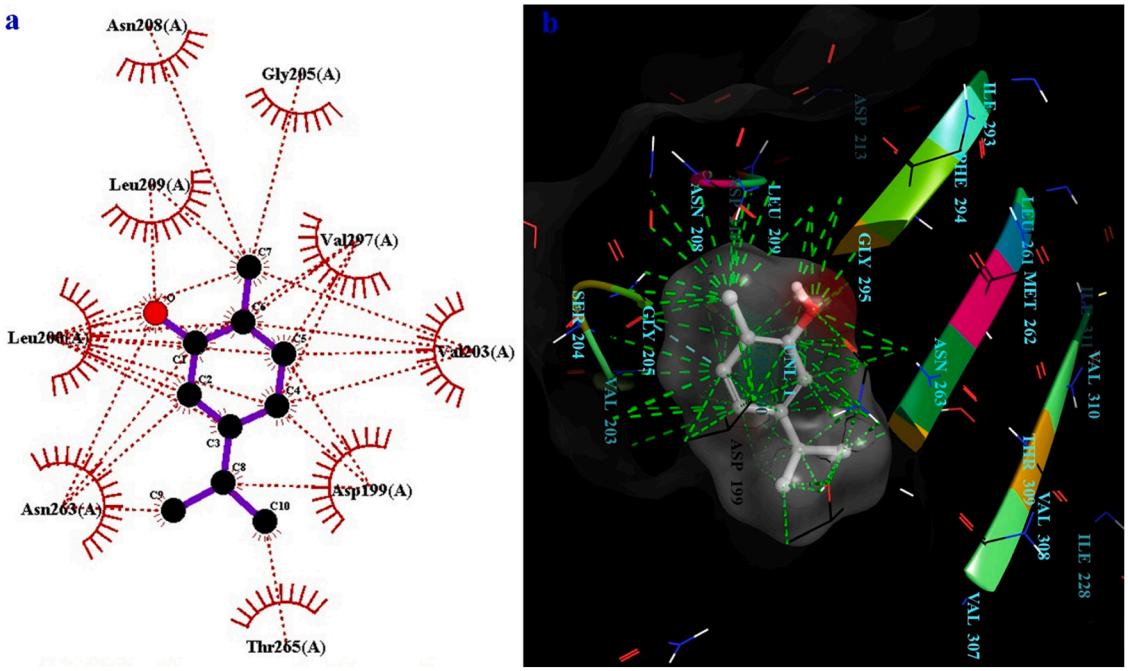

Fig. 5. (a) 2D interaction diagram and (b) 3D binding site representation of the 2OVZ-Carvacrol complex, showing hydrogen bonds (green dashed lines) and hydrophobic interactions (red arcs) with surrounding residues.

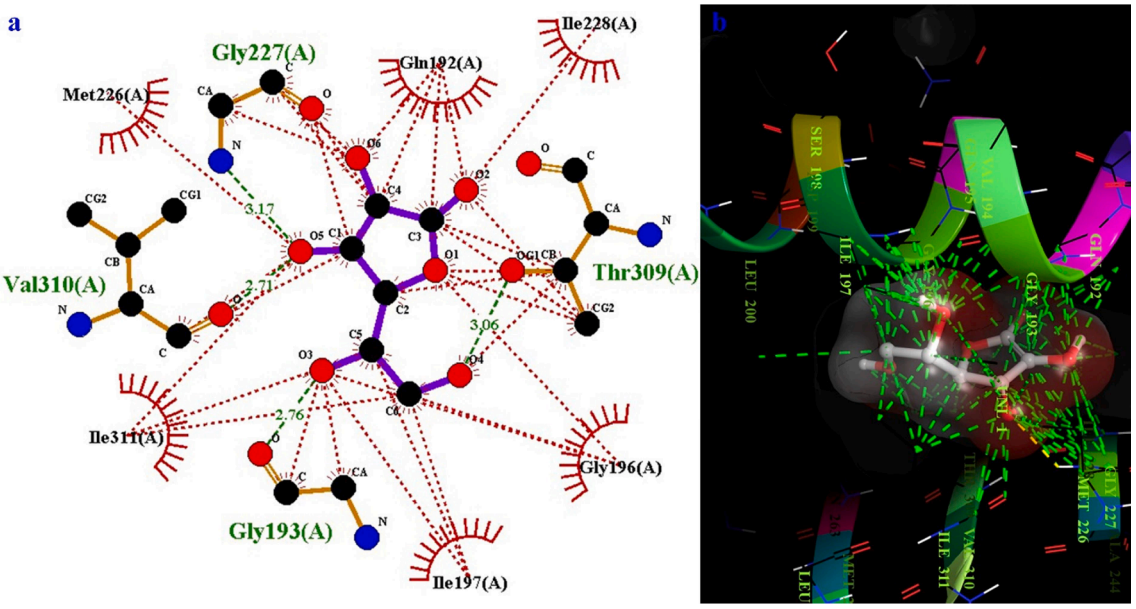

Fig. 6. (a) 2D interaction diagram and (b) 3D binding site view of the 2OVZ-Vitamin C complex, highlighting hydrogen bonds (green dashed lines) and hydrophobic contacts (red arcs) with key residues.

complex with the target protein, with strong hydrogen bonding and hydrophobic interactions playing a critical role in maintaining its binding pose. This stable interaction profile highlights Quercetin's potential as an effective ligand for this protein target Fig. 7.

3.6.2. *Carvacrol-protein complex*

The molecular dynamics simulation for the Carvacrol-protein complex was conducted over 100 nanoseconds at 300 K under an NPT ensemble. The Root Mean Square Deviation (RMSD) analysis provided insights into the stability of both the protein and the ligand throughout the simulation. Protein RMSD values remained within the typical 1–3 Å range, indicating stable conformational dynamics with minimal fluctuations. This stability suggests the protein maintained its structural integrity during the simulation. The ligand RMSD remained close to that of the protein, confirming that Carvacrol retained its binding orientation and did not drift from the binding site.

The Root Mean Square Fluctuation (RMSF) analysis showed that certain regions of the protein, particularly the N- and C-termini, displayed higher flexibility, while secondary structures like alpha-helices and beta-sheets were more rigid. Protein regions interacting directly

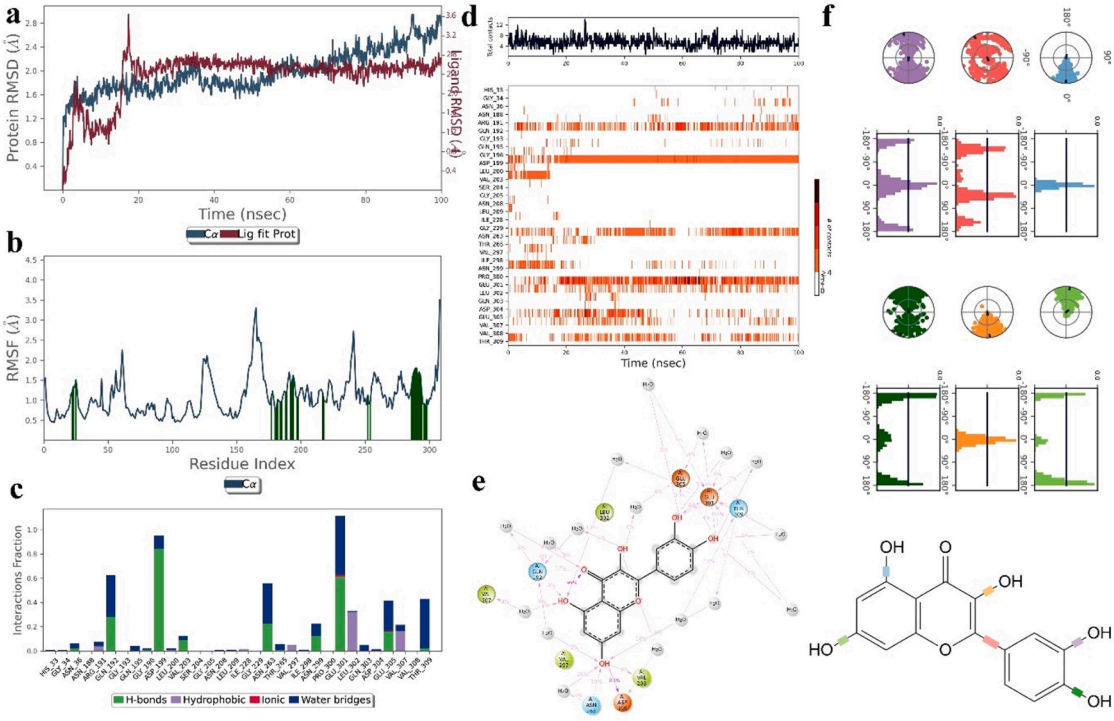

Fig. 7. (a) Protein RMSD, (b) RMSF, (c) interaction fraction, (d) contact timeline, (e) 2D interaction map, and (f) torsion profile for 2OVZ-Quercetin complex, highlighting stability and key interactions.

with Carvacrol exhibited lower RMSF values, indicating a stable binding environment around the ligand.

Analysis of protein-ligand interactions highlighted significant hydrogen bonding and hydrophobic interactions, which are essential for Carvacrol's binding stability. Hydrogen bonds were observed with residues such as Gly227 and Thr309, maintained for a substantial part of the simulation, thus reinforcing the ligand's binding affinity. Hydrophobic contacts, involving residues like Met226 and Val310, contributed to stabilizing Carvacrol in the binding pocket by creating a hydrophobic milieu around the ligand.

Protein secondary structure analysis revealed that the complex retained a balanced composition of alpha-helices and beta-strands, with a total secondary structure content of approximately 59.44 %. This stability in secondary structure further confirms the structural resilience of the protein during binding with Carvacrol.

The Ligand RMSF data indicated minimal fluctuation among Carvacrol's atoms, pointing to a rigid binding conformation with low internal flexibility. The torsion analysis of Carvacrol's rotatable bonds showed stable torsional angles throughout the simulation, suggesting that Carvacrol adopted a low-energy conformation within the protein's binding pocket.

In conclusion, Carvacrol forms a robust and stable complex with the target protein, largely due to consistent hydrogen bonds and hydrophobic interactions. These findings underscore Carvacrol's potential as a ligand with strong binding affinity, making it a promising candidate for further studies in drug design and development Fig. 8.

3.6.3. *Vitamin C -protein complex*

The molecular dynamics simulation of the Vitamin C-protein complex was conducted over a 100-nanosecond duration at 300 K in an NPT ensemble. The Root Mean Square Deviation (RMSD) for the protein indicated a stable structure, with values mostly within the 1–3 Å range, suggesting minimal structural fluctuations. This stability confirms that the protein reached equilibrium and maintained its native conformation throughout the simulation. The ligand RMSD, similarly, showed low fluctuations, indicating that Vitamin C remained stable within the protein's binding pocket without diffusing away from its initial binding site.

Analysis of the Root Mean Square Fluctuation (RMSF) highlighted that flexible region were concentrated in the terminal residues, as is typical in protein dynamics. Alpha-helices and beta-strands exhibited reduced fluctuations, while loop regions showed moderate flexibility. The binding site residues displayed minimal fluctuations, suggesting a rigid and stable environment for Vitamin C.

Protein-ligand interactions predominantly involved hydrogen bonds and hydrophobic contacts. Hydrogen bonds were observed with residues such as Thr190 and Gly228, maintained throughout a significant portion of the simulation, reinforcing Vitamin C's binding stability. Hydrophobic interactions, involving residues like Ile205 and Leu229, further stabilized Vitamin C within the binding pocket by creating a favorable non-polar environment. Additionally, water bridges mediated by nearby water molecules played a role in ligand stabilization, offering flexibility in binding dynamics.

Secondary structure analysis of the protein revealed that alpha-helices and beta-strands comprised around 58.93 % of the total structure, indicating structural integrity. Vitamin C's stability within the binding site was further supported by its RMSF, indicating limited movement of the ligand atoms.

The torsion analysis of Vitamin C's rotatable bonds demonstrated stability in torsional angles throughout the simulation, suggesting a low-energy conformation favorable for binding. This stability, along with low fluctuations in radius of gyration and solvent-accessible surface area, supported a compact and well-positioned binding pose.

Overall, the simulation results indicate that Vitamin C forms a stable and robust complex with the protein. The presence of consistent hydrogen bonds, hydrophobic interactions, and water-mediated contacts contributes to the strong binding affinity, underscoring Vitamin C's

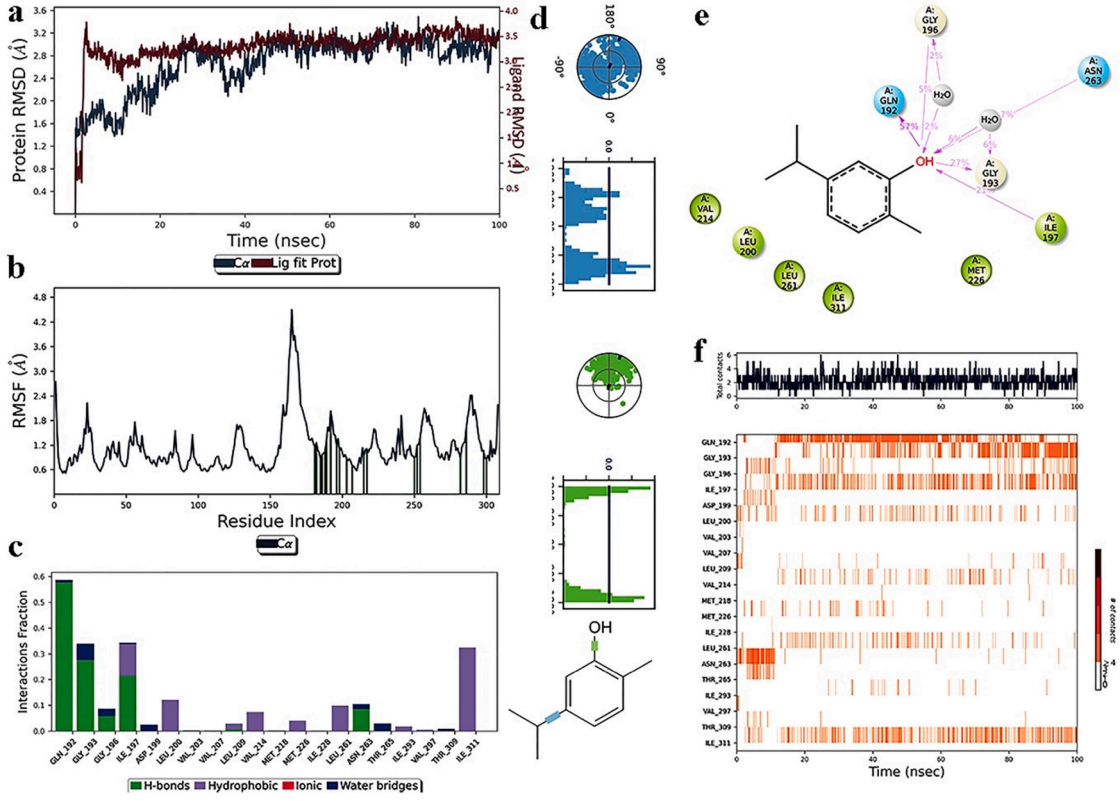

Fig. 8. (a) Protein RMSD, (b) RMSF, (c) interaction fraction, (d) contact timeline, (e) 2D interaction map, and (f) torsion profile for 2OVZ- Carvacrol complex, highlighting stability and key interactions.

potential as a reliable ligand for this protein target Fig. 9.

3.7. ADMET studies

The ADMET (Absorption, Distribution, Metabolism, Excretion, and Toxicity) analysis for three compounds: Quercetin, Carvacrol, a3.8nd Vitamin C is divided into four sections, labelled (a), (b), (c), and (d).

Sections (a), (b), and (c) each represent one of the compounds with their molecular structure and a radar chart visualizing various ADMET properties. The radar charts include parameters such as lipophilicity (LIPO), size, polarity (POLAR), solubility (INSOLU), flexibility (FLEX), and unsaturation (INSATU). These charts provide an overview of each compound's pharmacokinetic characteristics. For example, Quercetin shows a balanced profile with moderate lipophilicity and polarity, while Carvacrol has a higher lipophilicity, indicating more hydrophobic character. Vitamin C exhibits high polarity and solubility, characteristic of hydrophilic molecules. Section (d) presents a graphical summary of the compounds' predicted permeability and blood-brain barrier (BBB) penetration potential. The graph categorizes the compounds based on their log permeability surface area product (WLOGP) and topological polar surface area (TPSA), where Carvacrol is placed in a yellow zone, suggesting higher permeability and potential BBB penetration. In contrast, Quercetin and Vitamin C are positioned lower, indicating less BBB permeability. The color-coded legend in section (d) categorizes compounds based on different criteria like BBB penetration and human intestinal absorption (HIA). This ADMET profile provides valuable insights into the pharmacokinetic suitability of these compounds for drug development. Carvacrol, with its higher lipophilicity and BBB penetration potential, could be considered for neurological applications, while Quercetin and Vitamin C may be more suitable for systemic or topical applications where BBB penetration is not critical. The cardiac toxicity profiles of three compounds Quercetin, Carvacrol, and Vitamin C SMILES structure is listed, along with assessments for potential toxicities, including arrhythmia, cardiac failure, heart block, hERG toxicity, hypertension, and myocardial infarction Fig. 10.

Quercetin and Vitamin C are rated "Safe" across all categories, suggesting a low risk of cardiac toxicity. In contrast, Carvacrol is also deemed "Safe" in most categories but shows "Toxic" for hypertension. This indicates that Carvacrol may have a potential risk for inducing hypertension, whereas Quercetin and Vitamin C are safer options regarding cardiac-related side effects Fig. 11.

3.8. Soxhlet extraction

After the completion of extraction process the sample was concentrated in rotatory evaporator leaving out a slight yield of extracted sample of about 3.2 g (Suryowati et al., 2015). The yield efficiency was calculated using the formula (1) and found out to be 36 %.

$$Yield\ efficiency = \frac{Final\ weight\ of\ dried\ sample}{Initial\ weight\ taken\ for\ extraction} \times 100 \quad (4)$$

3.9. Synthesis and characterization of caesium carbonate nanoparticles

3.9.1. Central composite design

The ANOVA results for the quadratic model examining yield revealed a significant model fit (F-value = 33.94, $p < 0.0001$), confirming that the model can effectively describe the variation in yield. The significant model terms identified were (A^2), (B^2), and (C^2), representing the quadratic effects of calcium carbonate, caesium chloride, and *Coleus amboinicus* extract, respectively. These terms indicate that the response is influenced more by the nonlinear effects of these factors rather than their linear interactions or simple main effects, as indicated by the insignificance of the linear and interaction terms.

The model fit statistics were favorable, with an (R^2) of 0.9683 and an adjusted (R^2) of 0.9398, indicating that 96.83 % of the variability in yield was explained by the model. The predicted (R^2) of 0.7608, while slightly lower, was within 0.2 of the adjusted (R^2), showing reasonable predictability for the model. Adeq Precision, which measures the signal-to-noise ratio, was 13.032, well above the desirable threshold of 4, suggesting that the model provides a strong signal and is suitable for exploring the design space.

The final equation for yield in coded factors emphasized that the quadratic terms (A^2), (B^2), and (C^2) had substantial negative effects on yield, with coefficients of −8.39, −7.33, and −6.62, respectively. This suggests that increasing these factors beyond certain levels results in

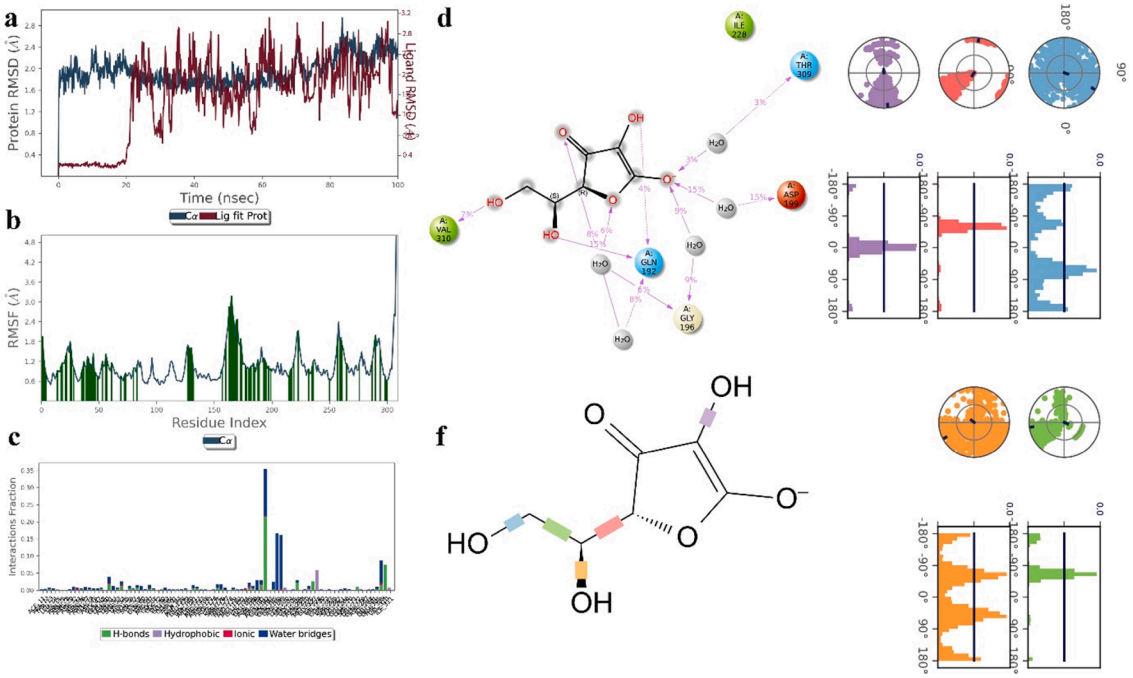

Fig. 9. (a) Protein RMSD, (b) RMSF, (c) interaction fraction, (d) 2D interaction map, (e) torsion profile, and (f) Vitamin C structure in 2OVZ-Vitamin C complex, showing stability and interaction details.

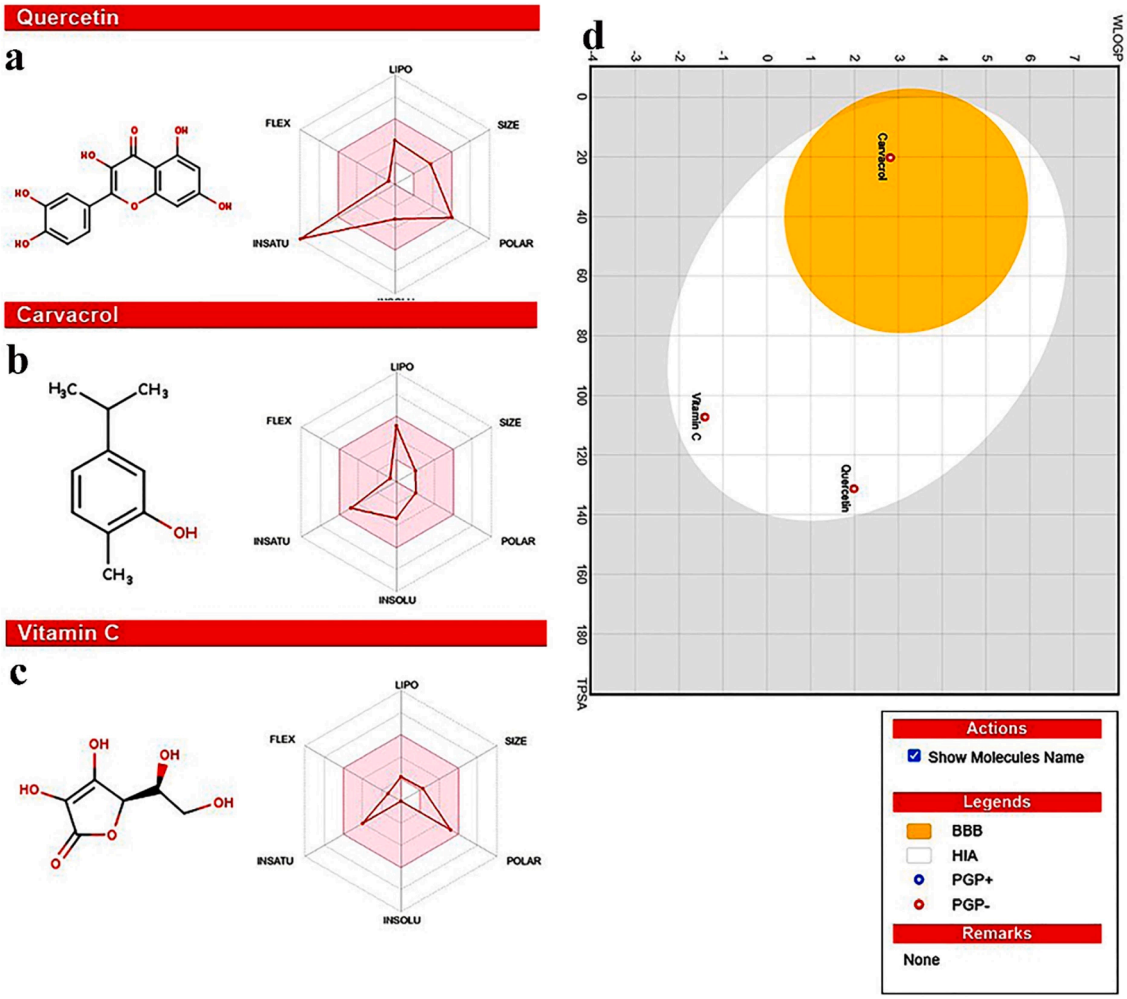

Fig. 10. (a-c) ADMET radar plots for Quercetin, Carvacrol, and Vitamin C. (d) BOILED-Egg plot indicating BBB penetration and gastrointestinal absorption. Yellow area represents high BBB penetration potential.

a

SMILES Quercetin	Arrhythmia	Cardiac Failure	Heart Block	hERG Toxicity	Hypertension	Myocardial Infarction
OC1=C(C2=CC=C(O)C(O)=C2)OC3=C(C(O)=CC(O)=C3)C1=O	Safe	Safe	Safe	Safe	Safe	Safe

b

SMILES Carvacrol	Arrhythmia	Cardiac Failure	Heart Block	hERG Toxicity	Hypertension	Myocardial Infarction
CC(C)C1=CC(O)=C(C)C=C1	Safe	Safe	Safe	Safe	Toxic	Safe

c

SMILES Vitamin C	Arrhythmia	Cardiac Failure	Heart Block	hERG Toxicity	Hypertension	Myocardial Infarction
OC([C@H](O1)[C@H](CO)O)=C(O)C1=O	Safe	Safe	Safe	Safe	Safe	Safe

Fig. 11. Cardiac toxicity profiles for Quercetin, Carvacrol, and Vitamin C. Green indicates "Safe" for cardiac events, while Carvacrol shows "Toxic" for hypertension, highlighting a potential cardiovascular risk.

diminishing returns or reductions in yield, highlighting the importance of optimization in this multivariable context.

Leverage and residual analyses indicated that the model performed consistently across different runs, with minimal residuals and leverage values in acceptable ranges. Internally and externally studentized residuals, along with Cook's distance and DFFITS, showed no indications of influential outliers, supporting the robustness of the model.

In summary, the quadratic model effectively captures the nonlinear relationship between the variables and yield. The significant quadratic terms suggest optimal ranges for each factor to maximize yield, as higher values tend to reduce the response. The strong statistical parameters (e.g., high (R^2), adequate precision) reinforce the model's suitability for predictive purposes, offering a reliable framework for yield optimization in practical applications involving calcium carbonate, caesium chloride, and *Coleus amboinicus* extract.

Equation

$$Yield = 92.15 + 0.0000 \cdot A + 0.0000 \cdot B + 0.0000 \cdot C + 0.0000 \cdot AB + 0.0000 \cdot AC + 0.0000 \cdot BC - 8.39 \cdot A^2 - 7.33 \cdot B^2 - 6.62 \cdot C^2 \quad (5)$$

This equation can be used to predict yield based on specific coded levels of each factor, where high levels are coded as +1 and low levels as −1.

The coefficients indicate the relative impact of each factor, with quadratic terms (A^2), (B^2), and (C^2) significantly affecting yield Fig. 12.

Solutions of 0.3M calcium carbonate and 0.3 M caesium chloride were prepared and mixed in a ratio of 1:1. 25 ml of coleus amboinicus plant extract was stirred in a beaker using a magnetic stirrer. The solution mixture is added drop wise to the plant extract and during this process; the stirring is continued until the desired colour gets decided. The beaker is removed from the magnetic stirrer and covered with aluminium foil, then incubated for approximately 24 h at room temperature (27 °C). The precipitate formed in the beaker is isolated and dried in a hot air oven. The vacuum-dried powder was subjected to further characterization.

3.10. Ultra violet – visible spectroscopy analysis

UV–VIS spectroscopy below shows that the obtained sample is indeed Caesium carbonate. The absorbance peak of the caesium carbonate nanoparticle was within the range of 200 to 800 nm. From the Fig. 13, the weak peaks at 290 nm and 490 nm reconfirmed the formation of Caesium carbonate nanoparticles Table 2.

3.11. Fourier transform infrared spectroscopy analysis

The FTIR spectrum of biosynthesized Cs_2CO_3 nanoparticles displayed distinct absorption bands, confirming the presence of functional groups derived from *Coleus amboinicus* phytochemicals that contribute to nanoparticle stabilization. A broad band at ~3390 cm^{-1} corresponds to O–H stretching vibrations of phenolic and alcoholic groups, indicative of polyphenols involved in the reduction and capping process. The peaks at 2921 cm^{-1} and 2852 cm^{-1} can be assigned to C–H stretching of aliphatic chains, likely originating from terpenoids. A prominent band near 1634 cm^{-1} is attributed to $C = O$ stretching in amide I or conjugated ketones, while the peak at 1540 cm^{-1} corresponds to N–H bending of amide II, suggesting the presence of proteins or peptides acting as stabilizing agents. The bands observed at 1384 cm^{-1} and 1246 cm^{-1} represent C–N stretching of aromatic amines and C–O stretching of phenolic compounds, respectively. Additionally, absorption at 1045 cm^{-1} is related to C–O–C stretching vibrations of ethers, while the bands at 874 cm^{-1} and 712 cm^{-1} correspond to carbonate group vibrations, confirming the presence of Cs_2CO_3. These results indicate that bioactive compounds in C. amboinicus play a dual role as reducing and capping agents, enhancing the stability and bioactivity of the synthesized nanoparticles (Fig. 14) (Table 3).

3.12. SEM analysis

The second SEM Fig. 15 confirmed the shape of the caesium carbonate nanoparticle is irregular hexagonal. It also helps to measure the particle size that is around 75–110 nm. SEM analysis is employed to examine the morphology of caesium carbonate nanoparticles

3.13. XRD analysis

X-Ray Diffraction Analysis is a powerful non-destructive method to characterise crystalline materials. It is a powerful technique for solving the crystal structure of materials. The appearance of metal alkali caesium carbonate nanoparticle is validated through XRD characterizations as mentioned in below Fig. 16, where specifically *Coleus amboinicus* has shown Again, from the Fig.ure5 nine abrasive peaks were seen which were correlated to given the crystal coordinates that are (001), (011), (111), (012), (112), (200), (113), (202) and (220). Therefore, the obtained caesium carbonate nanoparticle was investigated to be multi-planar hexagonal crystalline structure.

3.14. Anti-Oxidant assay

Coleus amboinicus leaf extract was used to synthesize caesium carbonate (Cs_2CO_3) nanoparticles and Anti-oxidant Assay was performed.

3.14.1. Total antioxidant assay

The total antioxidant assay was performed to determine the antioxidant properties of caesium carbonate nanoparticles. The bio formed Cs_2CO_3 showed a significant anti-oxidant property. Standard solution (Ascorbic acid) was used and graph was plotted. The concentration of unknown sample was 90.86 μg/ml Fig. 17 from standard graph.

3.14.2. DPPH radical scavenging assay

The biosynthesized Cs_2CO_3 nanoparticles demonstrated a concentration-dependent increase in free radical scavenging activity

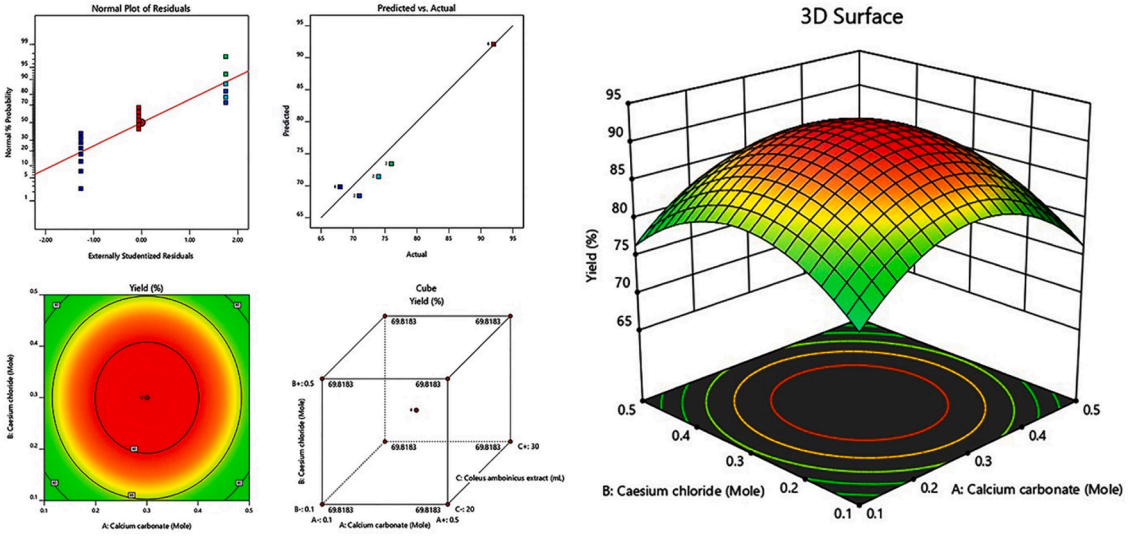

Fig. 12. Statistical analysis and optimization for yield: (top-left) normal plot of residuals, (center-left) predicted vs. actual yield, (bottom-left) contour plot, and (right) 3D response surface showing yield dependence on variables.

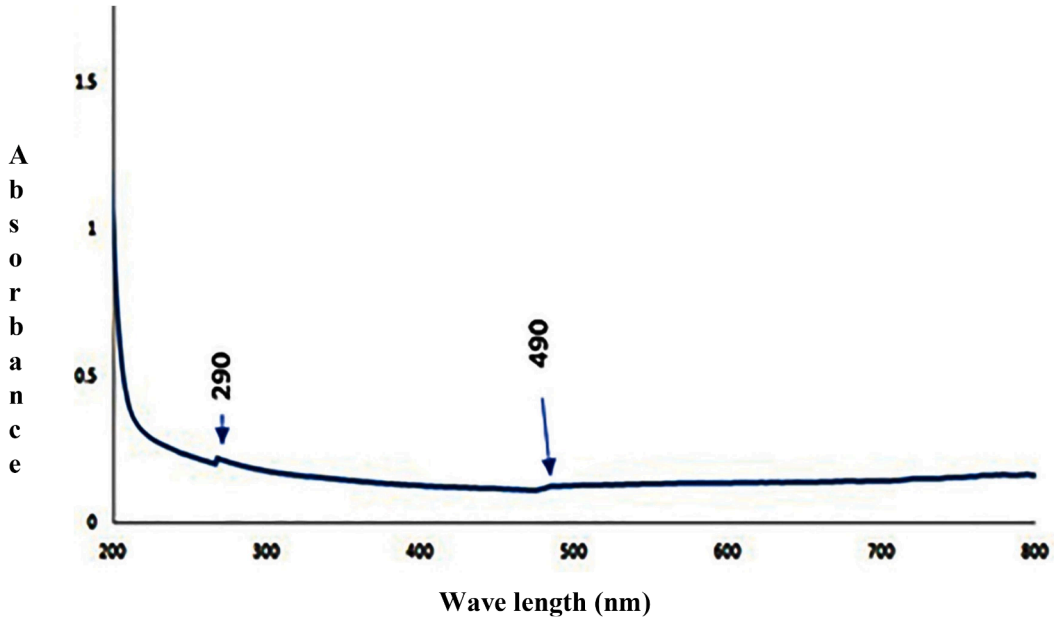

Fig. 13. UV–VIS absorption spectrum of caesium carbonate in the sample, showing prominent absorption peaks at 290 nm and 490 nm, indicating specific electronic transitions within the compound.

Table 2
Absorbance values at 680 nm for varying concentrations of sample. The table shows absorbance increasing with concentration, suggesting a dose-dependent relationship relevant for total antioxidant or similar assays.

S.No	Concentration	Absorbance at 680 nm
1	10	0.63
2	50	0.1
3	100	0.114
4	250	0.179
5	500	0.38

(**Supplementary Table 1**). Percentage inhibition rose from 32.61 ± 1.15 % at 10 μg·mL^{-1} to 89.43 ± 1.18 % at 500 μg·mL^{-1}, with an IC_{50} of 84.64 μg·mL^{-1} (Fig. 17). In comparison, the standard ascorbic acid showed markedly higher activity, achieving 86.77 ± 1.25 % inhibition at 500 μg·mL^{-1} with an IC_{50} of 28.01 μg·mL^{-1} (**Supplementary Table 2**) (Fig. 18). While this activity is notable, it was comparatively lower than that of the standard control, ascorbic acid, under identical assay conditions. This difference may be attributed to the higher radical-neutralizing capacity of ascorbic acid as a pure compound, compared to the nanoparticle-bound phytochemicals whose antioxidant activity may be influenced by surface accessibility and capping density [36]. Nevertheless, the relatively strong activity of Cs_2CO_3 NPs suggests that the phytochemical coating, particularly phenolic and flavonoid constituents from *Coleus amboinicus*, contributes significantly to free radical scavenging, making these nanoparticles promising candidates for antioxidant-based therapeutic applications.

One-way ANOVA followed by Tukey's post-hoc test revealed statistically significant differences ($p < 0.05$) between most concentration groups for both the nanoparticles and standard, confirming dose-dependent antioxidant potential. Similar antioxidant trends have been reported in other green nanomaterials. Cerium oxide nanoparticles synthesized using *Mentha royleana* extract also demonstrated significant DPPH, ABTS, and hydroxyl radical scavenging activity at higher doses [37]. These results reinforce the value of plant-mediated synthesis in preserving antioxidant capacity in nanomaterials and suggest that Cs_2CO_3 nanoparticles are promising eco-friendly agents in this arena.

3.15. Anti-inflammatory assay

Anti-inflammatory activity of bio synthesized caesium carbonate nanoparticles was evaluated by BSA inhibitory assay and Protease Inhibitory assay.

3.15.1. BSA inhibitory assay

The Cs_2CO_3 nanoparticles inhibited heat-induced protein denaturation in a concentration-dependent manner (**Supplementary Table 3**). Inhibition ranged from 34.29 ± 1.14 % at 10 μg·mL^{-1} to 45.61 ± 1.30 % at 500 μg·mL^{-1} Statistical analysis indicated significant differences ($p < 0.05$) between the lower and higher concentration groups, suggesting effective stabilization of protein structures. (Fig. 18).

3.15.2. Protease inhibitory assay

Protease inhibition by Cs_2CO_3 nanoparticles also increased with concentration, from 32.62 ± 1.18 % at 10 μg·mL^{-1} to 46.56 ± 1.28 % at 500 μg·mL^{-1}ANOVA and Tukey's post-hoc test revealed significant differences ($p < 0.05$) across most concentration pairs, supporting the nanoparticles' potential in suppressing proteolytic activity. (**Supplementary Table 4)** (Fig. 19).

Although specific reports on Cs_2CO_3 are scarce, analogous findings have emerged for other green-synthesized nanoparticles. Zinc oxide nanoparticles made using *Jasminum sambac* leaf extract demonstrated measurable anti-inflammatory activity *In vitro*, supporting the broader trend of phytogenic NP anti-inflammatory effects [38]. A recent review similarly emphasizes numerous plant-mediated metal and metal-oxide NPs that exhibit anti-inflammatory potential due to bioactive capping agents [39].These comparisons confirm that the observed bioactivity fits well within established green nanomedicine paradigms.

3.16. Antibacterial assay

The nanoparticles demonstrated notable antibacterial activity against both *E. coli* and *Staphylococcus aureus* (Table 4 and Fig. 20). For *E. coli*, inhibition zones increased from 2 ± 0.5 mm at 30 μg·mL^{-1} to 20 ± 0.8 mm at 60 μg·mL^{-1}. For *S. aureus*, the zones ranged from 5 ± 0.6 mm to 22 ± 0.9 mm over the same concentration range. While the standard antibiotic produced larger zones, statistical analysis confirmed significant differences ($p < 0.05$) between different nanoparticle

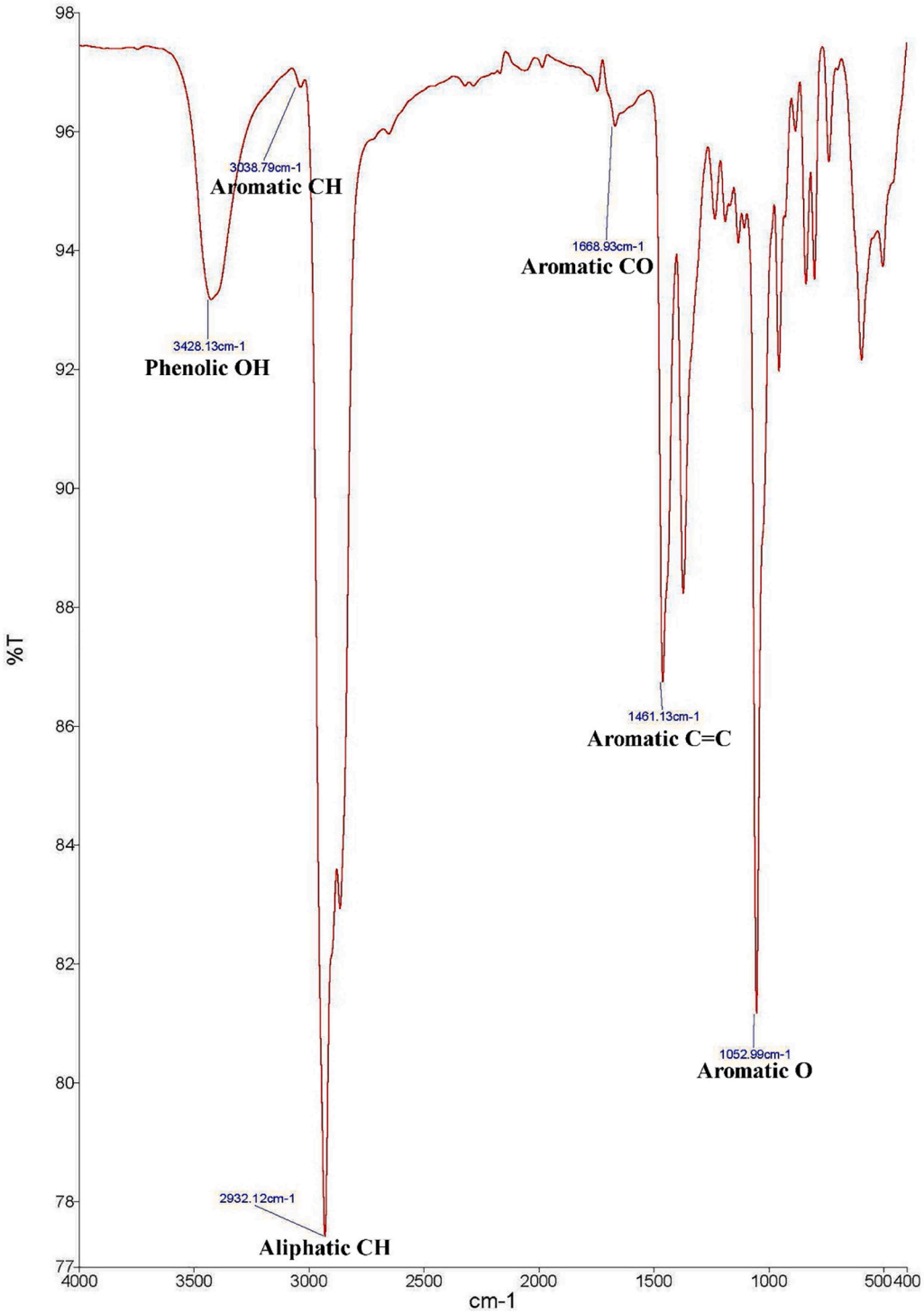

Fig. 14. FTIR spectrum showing absorbance peaks for functional groups in the sample, with major bands identified across the wavenumber range (4000–400 cm^{-1}), indicating chemical bonds and molecular composition of the sample.

concentrations, indicating a strong dose–response relationship. Cs_2CO_3 nanoparticles exhibited dose-dependent antibacterial effects, the efficacy approaching or surpassing some formulations of silver or zinc nanoparticles synthesized from plant extracts. Silver NPs from *Curcuma longa* flower extract generated zones of 22 mm against S. aureus and 13 mm against *E. coli*. Broader surveys also show that nanoformulations derived from medicinal plants like tulsi, turmeric, and Aloe vera demonstrate reliable antibacterial activity linked to their phytochemical components [40]. Interestingly, the NPs outperformed the control against *S. aureus*, suggesting enhanced efficacy against Gram-positive bacteria, potentially due to differences in cell wall structure that facilitate nanoparticle penetration and bioactive phytochemical interaction. The capping layer derived from *C. amboinicus* may also provide synergistic antimicrobial effects via disruption of bacterial membranes and interference with metabolic pathways. These results, when compared with the control, highlight that although Cs_2CO_3 NPs may not universally surpass conventional antibiotics in potency, they offer a sustainable and multifunctional antimicrobial alternative with potential for

Table 3
FTIR spectral peaks of Coleus amboinicus–mediated Cs_2CO_3 nanoparticles, indicating wavenumbers, associated functional groups, and their possible chemical assignments.

Peak Position (cm^{-1})	Functional Group	Possible Assignment
3428.13	O–H	Phenolic hydroxyl group
3368.79	C–H (aromatic)	Aromatic C–H stretching
2932.12	C–H (aliphatic)	Aliphatic C–H stretching
1688.83	$C = O$ (aromatic)	Aromatic carbonyl stretching
1461.13	$C = C$ (aromatic)	Aromatic $C = C$ stretching
1052.98	C–O (aromatic)	Aromatic C–O stretching

combination therapies.

3.17. In vitro anti TB screening

Herein we report anti TB screening of biosynthesized Cs_2CO_3 nanoparticles. After 7 days of incubation at 37 °C, the impact of these biosynthesized Cs_2CO_3 nanoparticles on the growth of MTB H37Ra was measured using the MABA method with concentrations of 0.97, 1.95, 3.90, 7.81, 15.62 and 31.25 $\mu g \cdot mL^{-1}$. Data of anti TB activity screening shows that biosynthesized Cs_2CO_3 nanoparticles were inactive at concentrations of 0.97, and 1.95 $\mu g \cdot mL^{-1}$ towards MTB H37Ra strain. Table 5 shows MABA results of Cs_2CO_3 nanoparticles (sensitive at 3.90, 7.81, 15.62 and 31.25 $\mu g \cdot mL^{-1}$). It is important to note that Cs_2CO_3 nanoparticles demonstrated higher activity and these compounds were used as a most potent analogue against several strains of microbes and shown to have similar anti TB potency.

4. Discussion

The *in silico* analysis revealed that quercetin, carvacrol, and vitamin C exhibited favourable binding energies and key interactions with the active site residues of MMP-9, suggesting potential inhibitory effects. This is particularly relevant as excessive MMP-9 activity is associated with inflammation, oxidative damage, and pathogenic bacterial survival [41]. The inclusion of these ligands in the in silico study is justified by their presence or structural similarity to compounds identified in *C. amboinicus*, which likely remain adsorbed on the Cs_2CO_3 nanoparticle surface post-synthesis [42]. These bioactive coatings could influence the nanoparticles' biological activities, complementing their intrinsic physicochemical properties [43]. Unlike purely descriptive docking reports, this approach critically links the molecular interactions observed in silico with the phytochemical–nanoparticle interface, providing a coherent rationale for their biological relevance and potential therapeutic applications [44].

Several recent studies have explored plant-mediated synthesis of metal and metal carbonate nanoparticles with comparable biomedical applications, providing useful experimental context for our findings [3]. Cost-effective and eco-friendly copper nanoparticles were synthesized using the leaf extract of *Dalbergia sissoo*, and their antibacterial, antioxidant, and anti-inflammatory activities were assessed [45]. *Catharanthus roseus* mediated CR-RuO2 NPs exhibited good scavenging activity, and effective anti-bacterial effect against *K. pneumonia* (21.6 ± 0.24 mm) [46]. *Mahonia bealei* mediated synthesis of strontium-doped SnO_2 nanoparticles exhibited notable antibacterial activity [19], while *Spirulina maxima* derived silver nanoparticles possessed broad-spectrum bactericidal properties [25]. ZnO nanoparticles synthesized using *Delphinium uncinatum* exhibited strong antioxidant and anti-inflammatory effects [28]. Our work aligns with these studies in adopting an eco-friendly, phytochemical-assisted approach, yet differs in employing *Coleus amboinicus* extract for the green synthesis of Cs_2CO_3 nanoparticles a route not previously reported. Additionally, the hexagonal crystalline morphology and particle size range observed in our study suggest distinct surface-interface properties that may influence biological performance. While these comparisons reinforce the plausibility of our results, differences in plant phytochemistry, nanoparticle composition, and assay conditions should be considered when interpreting cross-study trends. The findings of this study should be interpreted within the context of certain methodological and experimental constraints. All biological evaluations were conducted *In vitro*, and the absence of *In vivo* validation limits the ability to predict clinical or ecological outcomes. Second, no direct, side-by-side benchmarking was performed against previously reported nanoparticles under identical synthesis and assay conditions, which may influence the precision of comparative claims. The phytochemical profile of *Coleus amboinicus* extract, which functions as both the reducing and stabilizing agent, can vary depending on plant source, harvest season, and extraction parameters factors that could affect nanoparticle yield, morphology, and biological activity. The phytochemicals present in *Coleus amboinicus* extract play a pivotal role in the formation, stabilization, and functional performance of Cs_2CO_3 nanoparticles. FTIR analysis confirmed the presence of hydroxyl, carbonyl, amide, and terpenoid functional groups, which can interact with Cs^{2+} ions through hydrogen bonding, electrostatic attraction, and coordination complex formation. Phenolic –OH groups and carbonyl functionalities are likely to chelate with Cs^{2+}, reducing the

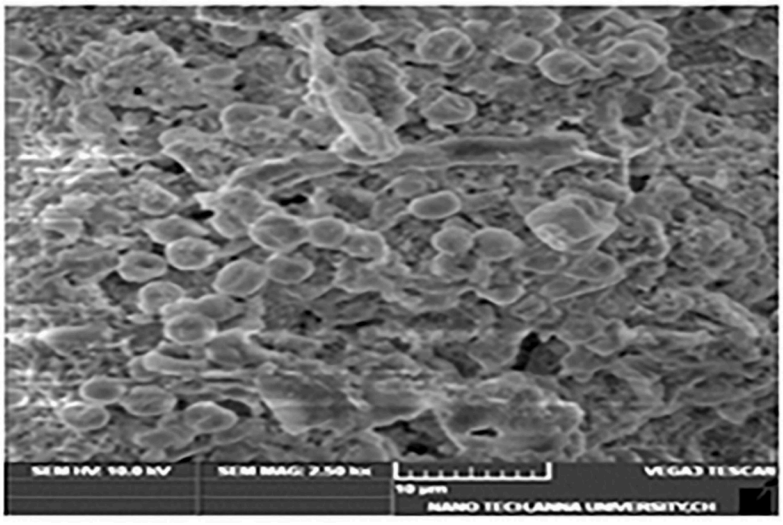

Fig. 15. Scanning Electron Microscopy (SEM) image showing the morphology of caesium carbonate nanoparticles, revealing a granular structure with spherical and irregularly shaped particles at 2.50k× magnification. Scale bar: 10 µm.

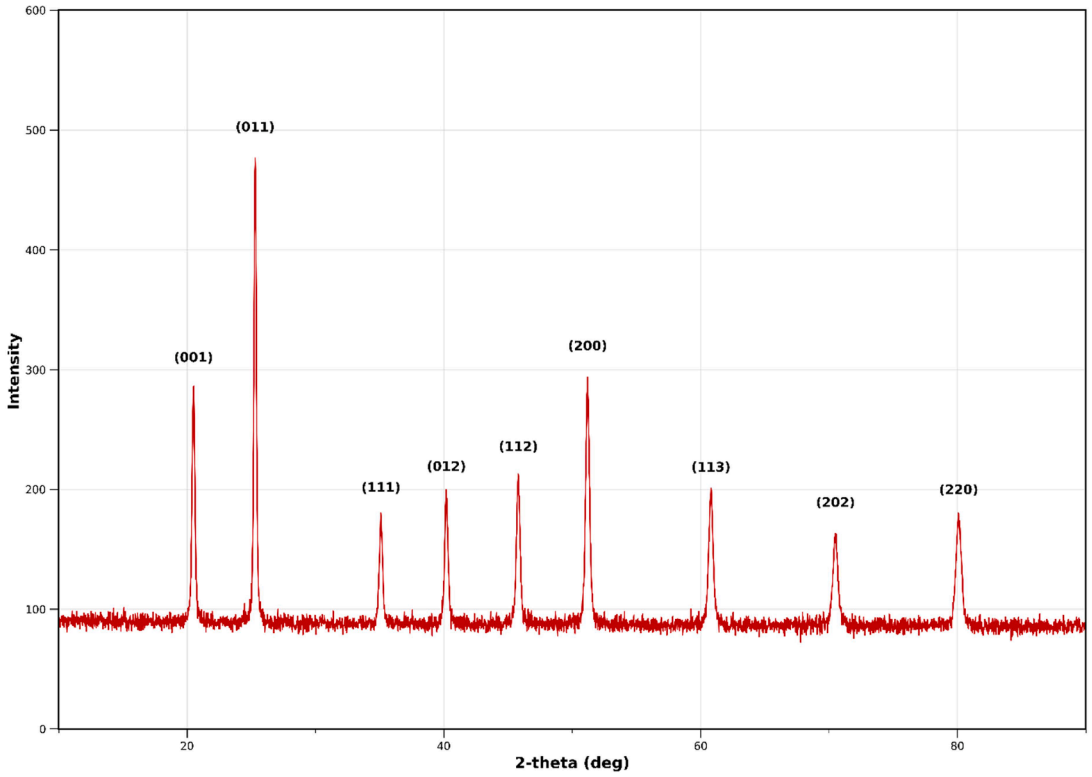

Fig. 16. X-ray diffraction (XRD) pattern of metal alkali caesium carbonate nanoparticles, displaying characteristic peaks at specific 2-theta values, confirming crystalline structure and phase identification of the nanoparticles.

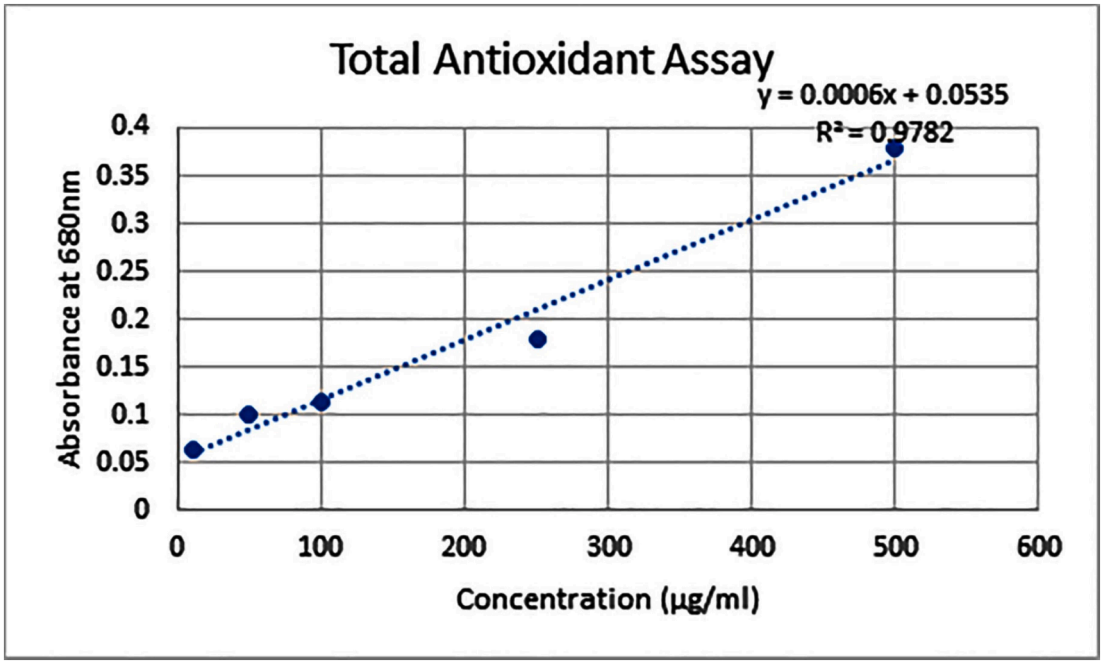

Fig. 17. Standard curve for ascorbic acid in the total antioxidant assay, showing a linear relationship between concentration (µg/ml) and absorbance at 680 nm.

precursor salt to Cs_2CO_3 while simultaneously forming a capping layer that inhibits particle aggregation. Terpenoids and amide-containing proteins may further contribute to steric stabilization and surface modification, resulting in nanoparticles with controlled morphology and size. This bio-organic corona enhances surface reactivity, potentially improving free radical scavenging by donating electrons or hydrogen atoms, suppressing enzyme activity via direct binding, and disrupting bacterial cell membranes by facilitating nanoparticle adhesion and penetration. These synergistic organic–inorganic interactions not only influence the physicochemical properties of Cs_2CO_3 NPs but also underpin their observed antioxidant, anti-inflammatory, and antimicrobial effects, aligning with similar reports on plant-mediated nanoparticle

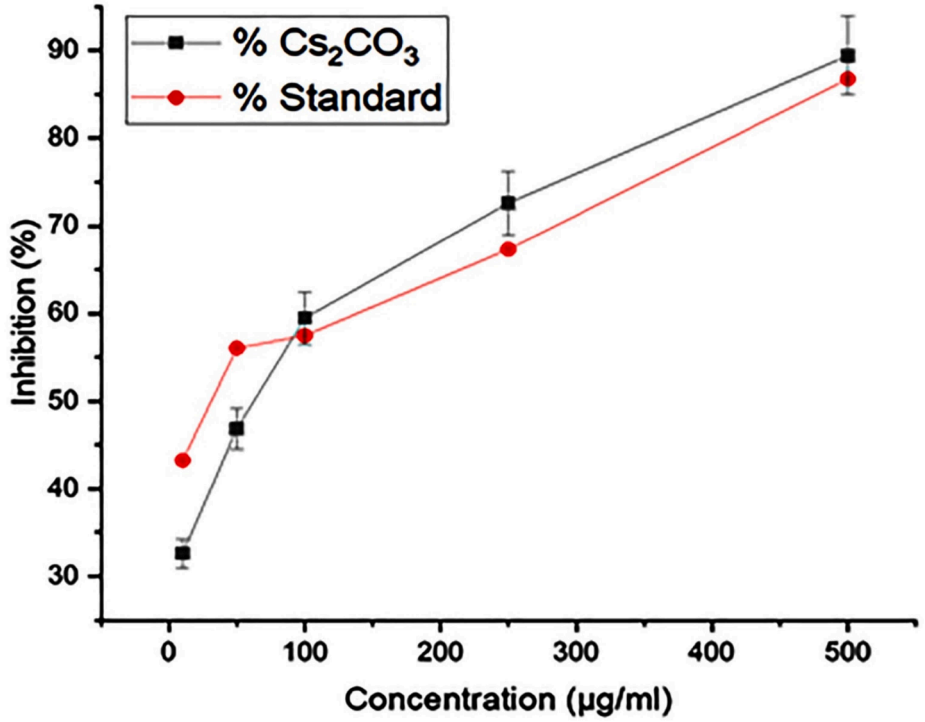

Fig. 18. DPPH assay comparing antioxidant activity of Cs_2CO_3 (black squares) and standard (red circles) at different concentrations. Results show similar antioxidant trends, with error bars indicating standard deviation.

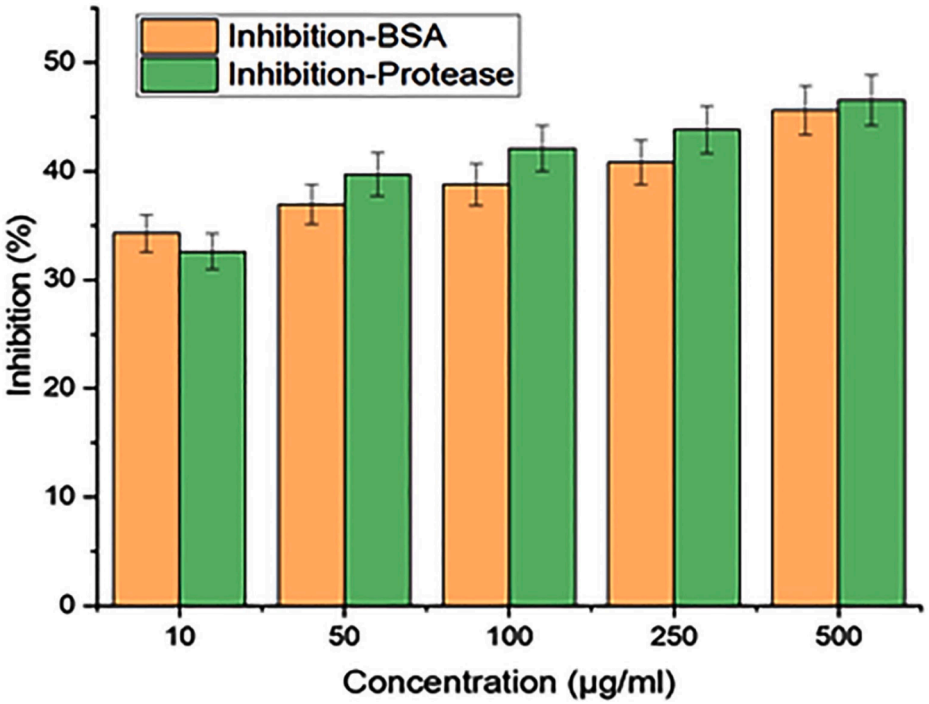

Fig. 19. Percentage inhibition of Cs_2CO_3 nanoparticles on BSA (orange) and protease (green). Bars represent inhibition at various concentrations, with error bars indicating standard deviation, showing comparative inhibition efficacy.

synthesis [47,48]. The antibacterial and antioxidant activities were tested under controlled laboratory conditions that may not fully replicate complex biological environments. These limitations are not supplementary considerations but essential parameters that recalibrate the interpretation and generalizability of our findings. Future studies incorporating standardized comparative assays, phytochemical profiling, and *In vivo* models will be critical for confirming the therapeutic relevance of *C. amboinicus* mediated Cs_2CO_3 nanoparticles.

5. Conclusion

This study demonstrates a natural green synthesis of Cs_2CO_3

Table 4
Antibacterial assay of biosynthesized Cs_2CO_3 nanoparticles showing zones of inhibition against *Escherichia coli* and Staphylococcus aureus at different concentrations, indicating dose-dependent antibacterial efficacy.

S. No	Cs_2CO_3 (µg/ml)	Zone of Inhibition *E. coli*	Zone of Inhibition *Staphylococcus aureus*
1	30	2 ± 0.5mm	5 ± 0.6mm
2	60	20 ± 0.8mm	22 ± 0.9mm
3	90	6 ± 0.6mm	8 ± 0.7mm
4	Std 30	17 ± 0.7mm	16 ± 0.7mm

nanoparticles using *Coleus amboinicus* leaf extract and the potential anticancer activity expressed by these nanoparticles where the plant extract has shown significant antioxidant, anti-inflammatory. Characterization data obtained include UV–Visible spectroscopy, FTIR and SEM which confirmed the structural integrity and morphology of the synthesized nanoparticles. The in silico molecular docking analysis reinforced our *In vitro* findings by revealing that key bioactive compounds present in the *Coleus amboinicus* extract, responsible for the capping and stabilization of Cs_2CO_3 nanoparticles, exhibited strong binding affinities toward target proteins linked to oxidative stress, inflammation, and microbial virulence. Docking scores ranged from –6.1 to –8.3 kcal·mol^{-1}, with interactions predominantly mediated by hydrogen bonding, hydrophobic forces, and π–π stacking, suggesting stable and specific protein–ligand complexes. Notably, the binding conformations indicated that these phytoconstituents could potentially modulate the active sites of enzymes relevant to antioxidant defence and protease inhibition, providing a plausible mechanistic basis for the observed bioactivities. Furthermore, ADMET profiling predicted acceptable oral bioavailability, low toxicity, and favourable pharmacokinetic characteristics, underscoring the translational potential of these nanoparticles in therapeutic applications. The integration of these in silico insights with our experimental results not only enhances the mechanistic understanding of nanoparticle bioactivity but also highlights their promise as multifunctional, eco-friendly nanomaterials for biomedical use. The *In vitro* antioxidant activities demonstrated through DPPH radical scavenging indicated their capacity to eliminate free radicals leading to the conclusion that they are potential candidates for treating diseases involving oxidative stress. The anti-inflammatory assays, especially BSA inhibition and protease inhibitory tests suggested an ability to suppress protein denaturation, a process involved in the management of chronic inflammation. The bactericidal activity against Gram-negative *E. coli* and Gram-positive *Staphylococcus aureus*, in addition, indicates the promising application of these nanoparticles as natural antibacterial agents that can be used to overcome the limitations associated with traditional antibiotics due to the emergence of resistant microorganisms. In conclusion, this study confirms the therapeutic potential of green synthesized Cs_2CO_3 nanoparticles from *Coleus amboinicus* against various health issues and emphasizes green synthesis available in nanotechnology. *In vivo* efficacy and safety could be studied in the future, opening avenues to develop sustainable bio-based nanomedicine for therapeutic applications targeting conditions complicated by oxidative stress, inflammation, and/or bacterial infections. However, for real-world translational application, further investigations are essential. These include comprehensive *In vivo* toxicity and biocompatibility evaluations, optimization of nanoparticle formulation for stability and delivery, and assessment under physiologically relevant conditions. Additionally, addressing the regulatory framework for green-synthesized nanomaterials will be crucial to ensure safety, efficacy, and compliance before clinical or commercial use. By integrating these future directions, the present findings serve as a foundation for advancing Cs_2CO_3 NPs toward practical biomedical deployment.

Funding

The authors are extending their appreciation to Deanship of

Table 5
Anti-TB activity of biosynthesized Cs_2CO_3 nanoparticles against MTB H37Ra. Sensitivity observed at concentrations ≥3.9 µg/mL, with highest activity at 31.25 µg/mL; inactive at lower concentrations.

Concentration (µg/mL)	Activity Against MTB H37Ra	Observation
0.0095	Sensitive	**Rifampicin(control)** Highest activity observed
0.97	Inactive	No activity observed
1.95	Inactive	No activity observed
3.9	Sensitive	Significant activity observed
7.81	Sensitive	Enhanced activity
15.62	Sensitive	Potent activity
31.25	Sensitive	Highest activity observed

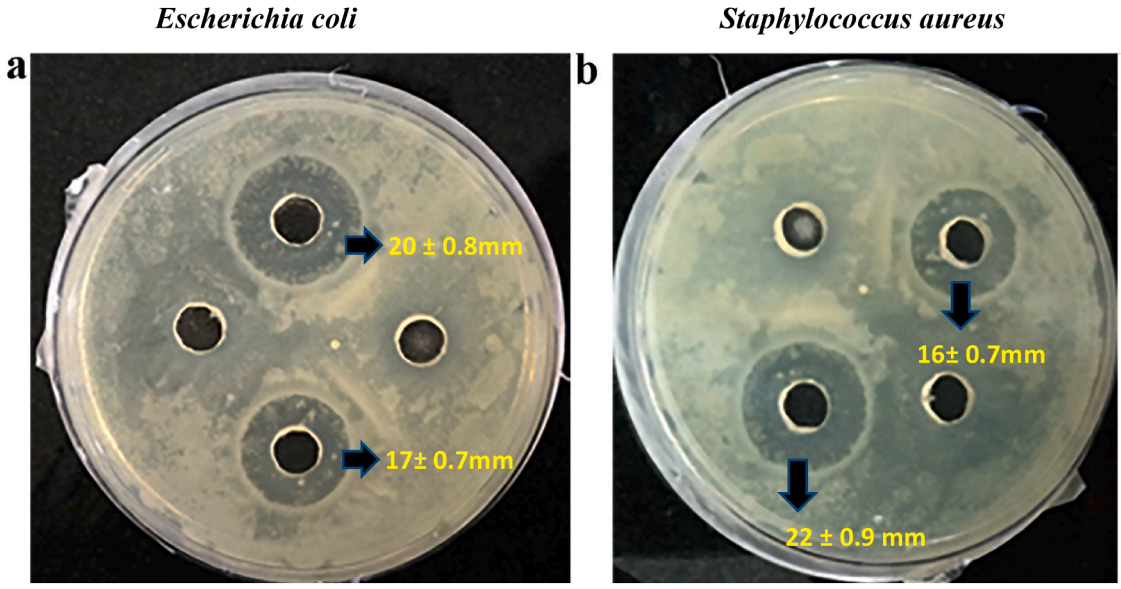

Fig. 20. Antibacterial assay of biosynthesized Cs_2CO_3 nanoparticles against (a) *Escherichia coli* and (b) *Staphylococcus aureus*, showing zones of inhibition, indicating antibacterial effectiveness on both bacteria.

Scientific research, for financial support through Ongoing Research Funding program (ORF-2025–354), King Saud University, Saudi Arabia.

CRediT authorship contribution statement

Yuvaraj Dinakarkumar: Writing – review & editing, Validation, Data curation, Conceptualization. **Panneerselvam Theivendren:** Validation, Software, Data curation. **Hamad Al Lohedan:** Funding acquisition. **Krishnakumar Ramya:** Validation, Investigation. **Kiruthika Jevanantham Senthamarai:** Investigation, Data curation. **Selvaraj Arokiyaraj:** Validation. **Jothi Ramalingam Rajabathar:** Funding acquisition.

Declaration of competing interest

The authors declare that they have no known competing financial interests or personal relationships that could have appeared to influence the work reported in this paper.

Acknowledgment

We would like to extend our heartfelt gratitude to the management and administration of all the institutions involved in this study. Dr. Jothi Ramalingam Rajabathar extend his appreciation to Deanship of Scientific research, for financial support through Ongoing Research Funding program (ORF-2025–354), King Saud University, Saudi Arabia.

Supplementary materials

Supplementary material associated with this article can be found, in the online version, at doi:10.1016/j.surfin.2025.107825.

Data availability

Data will be made available on request.

References

[1] M.K. Dewi, A.Y. Chaerunisaa, M. Muhaimin, I.M. Joni, Improved activity of herbal medicines through nanotechnology, Nanomaterials 12 (2022) 4073, https://doi.org/10.3390/nano12224073.
[2] D. Stan, A.-M. Enciu, A.L. Mateescu, A.C. Ion, A.C. Brezeanu, D. Stan, C. Tanase, Natural compounds with antimicrobial and antiviral effect and nanocarriers used for their transportation, Front. Pharmacol. 12 (2021) 723233, https://doi.org/10.3389/fphar.2021.723233.
[3] F. Gheisari, S.R. Kasaee, P. Mohamadian, S. Chelliapan, R. Gholizadeh, Z. Zareshahrabadi, S.P. Solhjoo, E. Vafa, S. Mosleh-Shirazi, A.M. Amani, Bromelain-loaded silver nanoparticles: formulation, characterization and biological activity, Inorg. Chem. Commun. 161 (2024) 112006, https://doi.org/10.1016/j.inoche.2023.112006.
[4] S. Aththanayaka, G. Thiripuranathar, S. Ekanayake, Emerging advances in biomimetic synthesis of nanocomposites and potential applications, Mater. Today Sustain. 20 (2022) 100206, https://doi.org/10.1016/j.mtsust.2022.100206.
[5] C. Verma, D.S. Chauhan, R. Aslam, P. Banerjee, J. Aslam, T.W. Quadri, S. Zehra, D. K. Verma, M.A. Quraishi, S. Dubey, Principles and theories of green chemistry for corrosion science and engineering: design and application, Green Chem. 26 (2024) 4270–4357, https://doi.org/10.1039/D3GC05207A.
[6] W. Zaman, A. Ayaz, S. Park, Climate change and medicinal plant biodiversity: conservation strategies for sustainable use and genetic resource preservation, Genet. Resour. Crop. Evol. (2025) 1–34, https://doi.org/10.1007/s10722-025-02410-2.
[7] S. Li, M. Dai, F. Wang, L. Hao, C. Feng, Y. Jia, Y. Li, X. Kang, X. Hu, H. Yan, PD-1/PD-L1 interaction upregulates YAP1 expression in hepG2 cells through MAPK/ERK pathway, Nat. Prod. Commun. 18 (2023), https://doi.org/10.1177/1934578X231210413, 1934578X231210413.
[8] Y. Man, C. Dai, Q. Guo, L. Jiang, Y. Shi, A novel PD-1/PD-L1 pathway molecular typing-related signature for predicting prognosis and the tumor microenvironment in breast cancer, Discover Oncol. 14 (2023) 59, https://doi.org/10.1007/s12672-023-00669-4.
[9] R.A. Laskowski, PDBsum 1: a standalone program for generating PDBsum analyses, Protein Sci. 31 (2022) e4473, https://doi.org/10.1002/pro.4473.
[10] A.M. Waterhouse, G. Studer, X. Robin, S. Bienert, G. Tauriello, T. Schwede, The structure assessment web server: for proteins, complexes and more, Nucleic. Acids. Res. (2024) gkae270, https://doi.org/10.1093/nar/gkae270.
[11] J.R. Mandhadi, T. Panneerselvam, P. Parasuraman, In DESIGN, silico modeling, toxicity study and synthesis of novel substituted semicarbazide derivatives of pyrimidine: an antitubercular agent, Curr. Bioact. Compd. 16 (2020) 294–301, https://doi.org/10.2174/1573407214666181001112601.
[12] C. Palanichamy, P. Pavadai, T. Panneerselvam, S. Arunachalam, E. Babkiewicz, S. Ram Kumar Pandian, K. Shanmugampillai Jeyarajaguru, D. Nayak Ammunje, S. Kannan, J. Chandrasekaran, Aphrodisiac performance of bioactive compounds from Mimosa pudica Linn.: in silico molecular docking and dynamics simulation approach, Molecules. 27 (2022) 3799, https://doi.org/10.3390/molecules27123799.
[13] T. Panneerselvam, S. Kunjiappan, S. Govindaraj, M. Gopal, K. Natarajan, Y. M. Hegde, N. Shanmugam, G. Srinivas, K. Ravi, V. Natarajan, Graph theoretical analysis, in silico modeling and molecular dynamic studies of (5-((2-chloropyridin-4-yl) oxy)-3-phenyl-1H-pyrazol-1-yl)-2-(4-substituted phenyl)-N, N-dimethylethen-1-amine derivatives for the treatment of breast cancer, AntiCancer Agents Med. Chem. (2022), https://doi.org/10.2174/1871520623666221205140328.
[14] R.R. Rajeshkumar, B.K. Kumar, P. Parasuraman, T. Panneerselvam, K. Sundar, D. N. Ammunje, S.R.K. Pandian, S. Murugesan, S.J. Kabilan, S. Kunjiappan, Graph theoretical network analysis, in silico exploration, and validation of bioactive compounds from Cynodon dactylon as potential neuroprotective agents against α-synuclein, BioImpacts: BI 12 (2022) 487, https://doi.org/10.34172/bi.2022.24113.
[15] G. Saravanan, T. Panneerselvam, S. Kunjiappan, P. Parasuraman, V. Alagarsamy, P. Udayakumar, M. Soundararajan, S.D. Joshi, S. Ramalingam, D.N. Ammunje, Graph theoretical analysis, in silico modeling, prediction of toxicity, metabolism and synthesis of novel 2-(methyl/phenyl)-3-(4-(5-substituted-1, 3, 4-oxadiazol-2-yl) phenyl) quinazolin-4 (3H)-ones as NMDA receptor inhibitor, Drug Dev. Res. 80 (2019) 368–385, https://doi.org/10.1002/ddr.21510.
[16] M. Sindhu, M. Poonkothai, R. Thirumalaisamy, Phenolic and terpene compounds from Plectranthus amboinicus (Lour.) Spreng. Act as promising hepatic anticancer agents screened through in silico and *In vitro* approaches, South Afr. J. Botany 149 (2022) 145–159, https://doi.org/10.1016/j.sajb.2022.06.006.
[17] A. Alqethami, A.Y. Aldhebiani, Medicinal plants used in Jeddah, Saudi Arabia: phytochemical screening, Saudi. J. Biol. Sci. 28 (2021) 805–812, https://doi.org/10.1016/j.sjbs.2020.11.013.
[18] J.R. Shaikh, M. Patil, Qualitative tests for preliminary phytochemical screening: an overview, Int. J. Chem. Stud. 8 (2020) 603–608, https://doi.org/10.22271/chemi.2020.v8.i2i.8834.
[19] A.S. Aloufi, Green synthesis of strontium-doped tin dioxide (SrSnO2) nanoparticles using the Mahonia bealei leaf extract and evaluation of their anticancer and antimicrobial activities, Green Processing and Synthesis, 12 (2023) 20228116. https://doi.org/10.1515/gps-2022-8116.
[20] R.D. Prasad, R.S. Prasad, R.B. Prasad, S.R. Prasad, S.B. Singha, D. Singha, R. J. Prasad, P. Sinha, S. Saxena, A.K. Vaidya, A review on modern characterization techniques for analysis of nanomaterials and biomaterials, ES Energy Environ. 23 (2024) 1087, https://doi.org/10.30919/esee1087.
[21] N. Fattahi, M. Kashif, A. Ramazani, Caesium carbonate functionalized magnetic nanoparticles: an efficient heterogeneous and reusable inorganic catalyst for aldol reaction in water, Inorganic Chemistry Communications, 149 (2023) 110388. https://doi.org/10.1016/j.inoche.2022.110388.
[22] A.E. Vladár, V.-D. Hodoroaba, Characterization of Nanoparticles By Scanning Electron microscopy, Characterization of Nanoparticles, Elsevier, 2020, pp. 7–27, https://doi.org/10.1016/B978-0-12-814182-3.00002-X.
[23] M.H. Ali, M.A.K. Azad, K. Khan, M.O. Rahman, U. Chakma, A. Kumer, Analysis of crystallographic structures and properties of silver nanoparticles synthesized using PKL extract and nanoscale characterization techniques, ACS. Omega 8 (2023) 28133–28142, https://doi.org/10.1021/acsomega.3c01261.
[24] F. Whba, F. Mohamed, N.R.A.M. Rosli, I.A. Rahman, M.I. Idris, The crystalline structure of gadolinium oxide nanoparticles (Gd2O3-NPs) synthesized at different temperatures via X-ray diffraction (XRD) technique, Radiation physics and chemistry, 179 (2021) 109212. https://doi.org/10.1016/j.radphyschem.2020.109212.
[25] R. Hanisha, M. Balaganapathy, B. Eswar, P. Kathirvelan, J.R. Rajabathar, N. Siddiqui, Y. Dinakarkumar, Biogenic synthesis of silver nanoparticles using Spirulina maxima extract and their bactericidal activity, J. Umm Al-Qura Univ. Appl. Sci. (2024) 1–11, https://doi.org/10.1007/s43994-024-00203-4.
[26] M. Locatelli, R. Gindro, F. Travaglia, J.-D. Coïsson, M. Rinaldi, M. Arlorio, Study of the DPPH-scavenging activity: development of a free software for the correct interpretation of data, Food Chem. 114 (2009) 889–897, https://doi.org/10.1016/j.foodchem.2008.10.035.
[27] K.H. Musa, A. Abdullah, A. Al-Haiqi, Determination of DPPH free radical scavenging activity: application of artificial neural networks, Food Chem. 194 (2016) 705–711, https://doi.org/10.1016/j.foodchem.2015.08.038.
[28] H. Rehman, W. Ali, N.Z. Khan, M. Aasim, T. Khan, A.A. Khan, Delphinium uncinatum mediated biosynthesis of zinc oxide nanoparticles and in-vitro evaluation of their antioxidant, cytotoxic, antimicrobial, anti-diabetic, anti-inflammatory, and anti-aging activities, Saudi. J. Biol. Sci. 30 (2023) 103485, https://doi.org/10.1016/j.sjbs.2022.103485.
[29] X. Zhao, L. Wang, M.Y. Xia, Z.C. Yang, Antimycobacterial compound of Cynoglossum lanceolatum Forsk.: bioassay guided isolation, molecular docking, synthesis of analogs, and a plausible mechanism of action, Chem. Biodivers. 20 (2023) e202200965, https://doi.org/10.1002/cbdv.202200965.
[30] P. Bhadwal, V. Randhawa, K. Vaiphei, D. Dahiya, N. Agnihotri, Clinical relevance of CERK and SPHK1 in breast cancer and their association with metastasis and drug resistance, Sci. Rep. 12 (2022) 18239, https://doi.org/10.1038/s41598-022-20976-0.

[31] P. Deng, Z. Shi, F. Fang, Y. Xu, L.-a. Zhou, Y. Liu, M. Jin, T. Chen, Y. Wang, Y. Cao, Wireless matrix metalloproteinase-9 sensing by smart wound dressing with controlled antibacterial nanoparticles release toward chronic wound management, Biosens. Bioelectron. 268 (2025) 116860, https://doi.org/10.1016/j.bios.2024.116860.
[32] D. Li, M. Wu, Pattern recognition receptors in health and diseases, Signal. Transduct. Target. Ther. 6 (2021) 291, https://doi.org/10.1038/s41392-021-00687-0.
[33] I. Luchian, A. Goriuc, D. Sandu, M. Covasa, The role of matrix metalloproteinases (MMP-8, MMP-9, MMP-13) in periodontal and peri-implant pathological processes, Int. J. Mol. Sci. 23 (2022) 1806, https://doi.org/10.3390/ijms23031806.
[34] G. Shankar, Y. Akhter, Molecular insights into ferric-siderophore transport by the putative TonB-dependent transporter in Mycobacterium tuberculosis, J. Biomol. Struct. Dyn. (2024) 1–18, https://doi.org/10.1080/07391102.2024.2368780.
[35] F.A. Binbay, D.C. Rathod, A.A.P. George, D. Imhof, Quality assessment of selected protein structures derived from homology modeling and AlphaFold, Pharmaceuticals 16 (2023) 1662, https://doi.org/10.3390/ph16121662.
[36] M.W. Alam, H.S. Al Qahtani, M. Aamir, A. Abuzir, M.S. Khan, M. Albuhulayqah, S. Mushtaq, N. Zaidi, A. Ramya, Phyto synthesis of manganese-doped zinc nanoparticles using carica papaya leaves: structural properties and its evaluation for catalytic, antibacterial and antioxidant activities, Polymers. (Basel) 14 (2022) 1827, https://doi.org/10.3390/polym14091827.
[37] M. Khan, R. Wali, Z.-u.-R. Mashwani, N.I. Raja, R. Ullah, A. Bari, S. Zaman, Sohail, Nanowarriors from mentha: unleashing nature's antimicrobial arsenal with cerium oxide nanoparticles, ACS. Omega 9 (2024) 15449–15462, https://doi.org/10.1021/acsomega.4c00562.
[38] S.J. Sugitha, R. Venkatesan, R.G. Latha, A.A. Vetcher, B.A. Al-Asbahi, S.-C. Kim, A study on the antibacterial, antispasmodic, antipyretic, and anti-inflammatory activity of ZnO nanoparticles using leaf extract from Jasminum sambac (L. Aiton), Molecules. 29 (2024) 1464, https://doi.org/10.3390/molecules29071464.
[39] H. Agarwal, A. Nakara, V.K. Shanmugam, Anti-inflammatory mechanism of various metal and metal oxide nanoparticles synthesized using plant extracts: a review, Biomed. Pharmacother. 109 (2019) 2561–2572, https://doi.org/10.1016/j.biopha.2018.11.116.
[40] S. Ghosh, S. Nandi, T. Basu, Nano-antibacterials using medicinal plant components: an overview, Front. Microbiol. 12 (2022) 768739, https://doi.org/10.3389/fmicb.2021.768739.
[41] H.S. Lee, W.J. Kim, The role of matrix metalloproteinase in inflammation with a focus on infectious diseases, Int. J. Mol. Sci. 23 (2022) 10546, https://doi.org/10.3390/ijms231810546.
[42] K. Paul, B.H. Gowda, U. Hani, R.S. Chandan, S. Mohanto, M.G. Ahmed, S. Ashique, P. Kesharwani, Traditional uses, phytochemistry, and pharmacological activities of Coleus amboinicus: a comprehensive review, Curr. Pharm. Des. 30 (2024) 519–535, https://doi.org/10.2174/0113816128283267240130062600.
[43] C.Y. Lee, S.M. Hu, J. Christy, F.Y. Chou, T.C. Ramli, H.Y. Chen, Biointerface coatings with structural and biochemical properties modifications of biomaterials, Adv. Mater. Interfaces. 10 (2023) 2202286, https://doi.org/10.1002/admi.202202286.
[44] M.K. Jayasinghe, C.Y. Lee, T.T. Tran, R. Tan, S.M. Chew, B.Z.J. Yeo, W.X. Loh, M. Pirisinu, M.T. Le, The role of in silico research in developing nanoparticle-based therapeutics, Front. Digit. Health 4 (2022) 838590, https://doi.org/10.3389/fdgth.2022.838590.
[45] S.M. Azharuddin, D. Chinna, K. Riazunnisa, Phytofabrication of copper oxide nanoparticles using Dalbergia sissoo leaf extract and evaluation of their biomedical applications, Next Res. (2025) 100571, https://doi.org/10.1016/j.nexres.2025.100571.
[46] S. Anjum, K. Riazunnisa, Fine ultra-small ruthenium oxide nanoparticles synthesis by using Catharanthus roseus and Moringa oleifera leaf extracts and their efficacy towards *In vitro* assays, antimicrobial activity and catalytic: adsorption kinetic studies using methylene blue dye, J. Clust. Sci. 33 (2022) 1103–1117, https://doi.org/10.1007/s10876-021-02037-0.
[47] J.K. Patra, G. Das, L.F. Fraceto, E.V.R. Campos, M.d.P. Rodriguez-Torres, L. S. Acosta-Torres, L.A. Diaz-Torres, R. Grillo, M.K. Swamy, S. Sharma, Nano based drug delivery systems: recent developments and future prospects, J. Nanobiotechnology. 16 (2018) 71, https://doi.org/10.1186/s12951-018-0392-8.
[48] P. Singh, Y.-J. Kim, D. Zhang, D.-C. Yang, Biological synthesis of nanoparticles from plants and microorganisms, Trends Biotechnol. 34 (2016) 588–599, https://doi.org/10.1016/j.tibtech.2016.02.006.